

# HOPS-dependent lysosomal fusion controls Rab19 availability for ciliogenesis in polarized epithelial cells

Huxley K. Hoffman<sup>1</sup> & Rytis Prekeris<sup>1,2\*</sup>

<sup>1</sup> Department of Cell and Developmental Biology, University of Colorado Anschutz Medical Campus, Aurora, CO 80045, USA.

<sup>2\*</sup> All correspondence should be addressed to [rytis.prekeris@ucdenver.edu](mailto:rytis.prekeris@ucdenver.edu).

*Running title:* HOPS controls Rab19 for cilia

*Key words:* cilia, epithelial polarity, HOPS complex, Rab19, renal epithelia, lysosomal fusion

*Summary statement:* Loss of HOPS-mediated lysosomal fusion indirectly blocks apical actin clearing and ciliogenesis in polarized epithelia by trapping Rab19 on late endosomes and depleting Rab19 from the basal body.

## ABSTRACT

Primary cilia are sensory cellular organelles crucial for organ development and homeostasis. Ciliogenesis in polarized epithelial cells requires Rab19-mediated clearing of apical cortical actin to allow the cilium to grow from the apically-docked basal body into the extracellular space. Loss of the lysosomal membrane-tethering HOPS complex disrupts this actin-clearing and ciliogenesis, but it remains unclear how ciliary function of HOPS relates to its canonical function in regulating late endosome-lysosome fusion. Here, we show that disruption of HOPS-dependent lysosomal fusion indirectly impairs actin-clearing and ciliogenesis by disrupting the targeting of Rab19 to the basal body. We also find that Rab19 functions in endolysosomal cargo trafficking apart from its previously-identified role in ciliogenesis. In summary, we show that inhibition of lysosomal fusion abnormally accumulates Rab19 on late endosomes, thus depleting Rab19 from the basal body and thereby disrupting Rab19-mediated actin-clearing and ciliogenesis.

*Abbreviations used:* HOPS, homotypic fusion and protein sorting; KO, knockout; LE, late endosome; LE/L, late endosome / lysosome, CORVET, class C core vacuole/endosome tethering; EE, early endosome; WT, wild-type; MDCK, Madin-Darby canine kidney; CQ, chloroquine; CA, constitutively active; V-ATPase, vacuolar-type ATPase; EEA1, early endosome antigen 1; IP, immunoprecipitation.

## 32 INTRODUCTION

33 The primary cilium is a sensory organelle, found on most types of cells in vertebrates, which is required for many of  
34 the key cellular signaling pathways that coordinate organ development and homeostasis (Anvarian et al., 2019;  
35 Goetz and Anderson, 2010; Wheway et al., 2018). Mutations in genes involved in primary cilia formation and  
36 function produce genetic disorders termed ciliopathies, affecting multiple organ systems (Hildebrandt et al., 2011;  
37 Mitchison and Valente, 2017; Reiter and Leroux, 2017). Renal disease is a prominent feature of many ciliopathies,  
38 as defects in the primary cilia of the polarized epithelial cells that line the renal tubules lead to development of  
39 kidney cysts and loss of kidney function (Devlin and Sayer, 2019; McConnachie et al., 2021). For example,  
40 autosomal dominant polycystic kidney disease, the most common inherited cause of kidney failure, is caused by  
41 loss-of-function mutations in a ciliary receptor complex (McConnachie et al., 2021). This makes it important to  
42 understand the mechanisms underlying cilia formation in polarized epithelial cells.

43 Primary ciliogenesis involves extension of a microtubule-based axoneme from a basal body which  
44 develops from the mother centriole (Pedersen et al., 2008). The ciliogenesis process shows some mechanistic  
45 differences in polarized epithelial cells as compared to other cell types (Hoffman and Prekeris, 2022; Molla-Herman  
46 et al., 2010; Sorokin, 1968). In most cell types, the primary cilium initially develops within an intracellular ciliary  
47 vesicle which later fuses with the plasma membrane to expose the tip of the cilium to the extracellular space, but in  
48 polarized epithelial cells, it appears that the basal body first docks at the apical plasma membrane and then  
49 extends the cilium directly into the extracellular space. An important early step in this process is the formation of a  
50 clearing in the apical actin cortex (actin clearing) to allow the basal body docking and protrusion and growth of the  
51 ciliary axoneme (Hoffman and Prekeris, 2022; Jewett et al., 2021).

52 Previous work from our lab (Jewett et al., 2021) identified Rab19 GTPase and the homotypic fusion and  
53 protein sorting (HOPS) tethering complex as being both required for this apical actin cortical clearing step during  
54 ciliogenesis in renal polarized epithelial cells. Rab19 localizes to the site of actin clearing, and knockout (KO) of  
55 either Rab19 or the HOPS subunit Vps41 disrupts actin clearing and ciliogenesis. Another HOPS subunit, Vps39,  
56 has also been implicated in the regulation of ciliogenesis in renal cells (Iaconis et al., 2020), and all subunits of the  
57 HOPS complex were identified in a functional genomic screen for regulators of ciliary signaling (Breslow et al.,  
58 2018). The HOPS complex was also shown to be a Rab19 effector, i.e. HOPS interacts with Rab19 in its GTP-  
59 bound active state (Jewett et al., 2021).

60 Rab GTPases in general act as molecular switches that control intracellular membrane trafficking pathways  
61 (Homma et al., 2021; Stenmark, 2009), but specific roles of Rab19 apart from its requirement in ciliogenesis remain  
62 largely unknown. Among the scarce clues to the overall cellular functions of Rab19 is that the Rab19 ortholog in  
63 *Drosophila* localizes to the Golgi (Sinka et al., 2008). The HOPS complex, however, has a well-established role in  
64 lysosomal trafficking, where it serves as a membrane tethering complex for fusion of late endosomes (LEs),  
65 autophagosomes, and AP-3 vesicles to lysosomes (hereafter referred to collectively as lysosomal fusion)  
66 (Balderhaar and Ungermann, 2013; Jiang et al., 2014). Since Rab19 showed little localization to LEs or lysosomes,  
67 it was proposed that Rab19 is not involved in lysosomal trafficking and that HOPS interacts with Rab19 to mediate  
68 actin clearing and ciliogenesis through a non-lysosomal pathway (Jewett et al., 2021). However, the mechanism by  
69 which HOPS regulates ciliogenesis, and whether Rab19 binding to HOPS is directly involved in apical actin  
70 clearance, remains unknown.

71 In this study, we investigated the role of the HOPS complex in actin cortical clearing and primary  
72 ciliogenesis. We found that pharmacological inhibition of lysosomal fusion produces similar defects in actin-clearing  
73 and ciliogenesis as Vps41 KO, suggesting that the requirement for HOPS in ciliogenesis is a consequence of its  
74 requirement in lysosomal trafficking, as opposed to representing a direct non-lysosomal function of HOPS at the  
75 basal body. We furthermore found that inhibiting lysosomal fusion impairs ciliogenesis not simply by blocking the  
76 degradation of ciliogenesis inhibitors, but rather by disrupting the regulation and localization of key ciliogenesis  
77 machinery i.e. Rab19. Additionally, we discovered that Rab19 interacts not only with the late endosome/lysosome  
78 (LE/L)-associated HOPS complex but also with the related early endosome (EE)-associated class C core  
79 vacuole/endosome tethering (CORVET) complex, and we found that CORVET-containing EEs (in contrast to  
80 HOPS-containing LE/Ls) may be directly involved at the basal body in the process of ciliogenesis. Finally, we also  
81 found evidence for a previously-uncharacterized role for Rab19 in endolysosomal trafficking. In summary, this study  
82 suggests that Rab19 has at least two distinct functions: (1) regulating lysosomal protein traffic; and (2) regulating  
83 apical actin clearance and cilia formation in polarized epithelial cells. In contrast, HOPS-depletion appears to affect  
84 cilia formation indirectly, predominately by trapping Rab19 on enlarged LEs away from the apically-localized basal  
85 body.

86

## 87 **RESULTS**

88

### 89 **Disruption of lysosomal fusion impairs apical actin clearing and primary ciliogenesis**

90 The HOPS complex was originally identified as a regulator of lysosomal trafficking, acting as a membrane tether to  
91 mediate lysosomal fusion (Balderhaar and Ungermann, 2013; Jiang et al., 2014; Seals et al., 2000; Wartosch et al.,  
92 2015). Thus, it might be that HOPS affects ciliation by affecting the lysosomal degradation pathway, or alternatively  
93 it might be that HOPS has an additional non-lysosomal function in directly mediating traffic to and from the basal  
94 body. Consistent with the former possibility, it has been reported that autophagic degradation of several ciliation  
95 inhibitors is needed for primary cilia formation (Liu et al., 2021; Tang et al., 2013; Yamamoto and Mizushima, 2021;  
96 Yamamoto et al., 2021). Thus, we first assessed whether the requirement for the HOPS complex in actin cortical  
97 clearing and ciliogenesis was related to, or independent of, the role of HOPS in lysosomal fusion. To address this  
98 question, we tested whether pharmacological inhibition of lysosomal fusion would produce the same defects in  
99 actin clearing and ciliogenesis as Vps41 KO. Chloroquine (CQ) is a lysosomal inhibitor which impairs lysosomal  
100 fusion (Mauthe et al., 2018; Mullock et al., 1998), making it a good candidate to pharmacologically mimic the  
101 lysosomal fusion defect of Vps41 KO.

102 We first tested whether CQ treatment had similar effects on the lysosomal pathway as Vps41 KO. We  
103 compared the morphology of acidic organelles, i.e. LE/Ls, in Vps41 KO Madin-Darby canine kidney (MDCK) cells to  
104 CQ-treated and untreated control wild-type (WT) MDCK cells. LysoTracker dye was used to label all acidic  
105 organelles including LE/Ls. Both Vps41 KO and CQ treatment produced a dramatic increase in the size of  
106 LysoTracker-positive LE/Ls (Fig. 1A,B). These enlarged LysoTracker compartments likely represent stalled LEs,  
107 which have acidified enough for LysoTracker staining, but have failed to fuse to a mature lysosome to degrade their  
108 contents and therefore accumulate an abnormal volume of excess cargo. This result supports that CQ treatment  
109 has similar effects on the lysosomal pathway as Vps41 KO.

110 We then used CQ as a tool to test whether inhibition of lysosomal fusion was sufficient to cause defects in  
111 apical actin clearing and ciliogenesis like those observed in Vps41 KO MDCK cells. The reduction in cortical actin  
112 above the basal body relative to flanking regions of the apical actin cortex (Fig. 1C-E), and the percent of cells  
113 exhibiting a primary cilium after 3 days of culture as confluent monolayers (Fig. 1F,G), were compared between  
114 untreated control, CQ-treated, and Vps41 KO cells. Ciliation was assessed after 3 days because cells could  
115 withstand this duration of 10  $\mu$ M CQ without major impacts to cell survival and morphology; the early time point  
116 accounts for the low rate of ciliation in WT MDCK as compared to the prior study where ciliation was assessed after  
117 8 days (Jewett et al., 2021). Actin clearing and ciliation were similarly impaired in both Vps41 KO and CQ-treated  
118 cells (Fig. 1C-G), indicating that pharmacological inhibition of lysosomal fusion recapitulates the Vps41 KO defects  
119 in these processes. These findings suggest that the apical actin-clearing and ciliogenesis defects of Vps41 KO  
120 MDCK are likely due to the loss of the canonical HOPS complex function as a membrane tether for lysosomal  
121 fusion, rather than reflecting a separate non-lysosomal function of the HOPS complex.

122 The clearing in the apical actin cortex around the base of the cilium, besides being important to allow for  
123 basal body docking and axoneme extension during ciliogenesis (Jewett et al., 2021), has also been shown to  
124 regulate the exclusion of non-ciliary apical membrane proteins such gp135 (Francis et al., 2011). Consistent with  
125 this, in CQ-treated cells as in Vps41 KO cells where actin clearing was defective, the clearing of gp135 was  
126 similarly lost (Fig. 2A). Since both actin clearing and ciliation were reduced but not completely abolished in Vps41  
127 KO and CQ-treated cells, we wondered whether the cilia that did form in these conditions formed within actin  
128 clearings, or whether these were cilia aberrantly extended through an intact apical actin cortex. Although the  
129 clearing of basal-body-associated cortical actin is impaired in the majority of Vps41 KO and CQ-treated cells, a few  
130 cells in these conditions still exhibit normal actin clearing (Fig. 2B), and when cilia were observed in Vps41 KO and  
131 CQ-treated cells, they were associated with actin clearings (Fig. 2C). Thus, the occasional cilia found in Vps41 KO  
132 or CQ-treated cells represent the occasional cells in which actin clearing was successful, not cells where  
133 ciliogenesis proceeded without actin clearing, further demonstrating that ciliogenesis is tightly coupled to actin  
134 cortical remodeling. While cilia were typically not found without actin clearings, in contrast, actin cortical clearings  
135 without detectable ciliary axonemes were frequently observed (Fig. 1C and Fig. 2D), supporting the model in which  
136 actin cortical clearing is required at an early stage of ciliogenesis prior to axoneme extension (Jewett et al., 2021)  
137 and thus the actin-clearing defect of Vps41 KO or CQ-treated cells is presumably a cause, as opposed to a  
138 consequence, of the ciliation defect.

139

#### 140 **Ciliation defect of Vps41 KO MDCK is not due to impaired degradation of MYH9, OFD1, or CP110**

141 Previous research has found that autophagy promotes primary ciliogenesis by selectively degrading certain  
142 negative regulators of ciliogenesis, including MYH9 (Yamamoto et al., 2021), OFD1 (Tang et al., 2013), and CP110  
143 (Liu et al., 2021). Autophagic degradation relies on HOPS-mediated autophagosome-lysosome fusion (Jiang et al.,  
144 2014), and is therefore expected to be impaired by Vps41 KO. We confirmed that Vps41 KO MDCK cells show  
145 elevated levels of the autophagosome marker LC3B-II reflecting some defects in autophagic degradation (Fig.  
146 S1A,B). We therefore wondered whether the ciliogenesis defects observed in Vps41 KO were due to impaired  
147 degradation of MYH9, OFD1, or CP110. MYH9 was reported to inhibit ciliogenesis by stabilizing actin (Rao et al.,  
148 2014; Yamamoto et al., 2021), making it particularly likely that a lack of degradation of MYH9 could account for the  
149 actin-cortical-clearing defect. We therefore examined MYH9 localization (Fig. S1C) and protein levels (Fig. S1D,E)

150 in Vps41 KO MDCK. If MYH9 were an autophagy cargo and its degradation were blocked by Vps41 KO, then  
151 undegraded MYH9 would be expected to accumulate in autophagosomes leading to an overall increase in MYH9  
152 protein levels. We did not observe accumulation of GFP-MYH9 in LC3B-labeled autophagosomes in Vps41 KO  
153 MDCK cells or in MDCK cells treated with the autophagy inhibitor Bafilomycin A1 (BafA) (Fig. S1C), nor were  
154 MYH9 levels significantly altered in Vps41 KO MDCK (Fig. S1D,E), suggesting that MYH9 does not appear to be an  
155 autophagy cargo in MDCK cells under the conditions of these experiments. We also examined the effects of GFP-  
156 MYH9 overexpression in WT MDCK cells and found that elevated levels of MYH9 did not block actin clearing or  
157 ciliation in these cells (Supp Fig. S1F). Thus, contrary to previous reports in RPE1, IMCD3 cells (Rao et al., 2014),  
158 and MEFs (Yamamoto et al., 2021), MYH9 did not appear to be a ciliogenesis inhibitor in MDCK cells. Vps41 KO  
159 also showed little effect on cellular OFD1 or CP110 protein levels (Fig. S1D,E). Our data therefore did not support  
160 the hypothesis that the actin-clearing and ciliogenesis defects of Vps41 KO cells were due to impaired autophagy of  
161 MYH9, OFD1, or CP110.

162

### 163 **Disruption of lysosomal fusion impairs ciliogenesis by retaining Rab19 on enlarged LEs and sequestering** 164 **it away from the basal body**

165 Since Rab19 interacts with the HOPS complex and functions in actin cortical clearing and ciliogenesis (Jewett et  
166 al., 2021), we wondered whether the ciliogenesis defects caused by inhibition of lysosomal fusion were due to an  
167 effect on Rab19. We therefore examined whether Rab19 localization was altered in Vps41 KO or CQ-treated cells.  
168 As previously reported (Jewett et al., 2021), in WT MDCK, Rab19 vesicles were enriched around the basal body  
169 and actin clearing site (Fig. 3A,B), and Rab19 showed little localization to LE/Ls (Fig. 3C,D). We also observed a  
170 substantial pool of Rab19 in the Golgi (Fig. S2A,B), consistent with the reported Golgi localization of Rab19 in  
171 *Drosophila* (Sinka et al., 2008). Although the Golgi apparatus localizes around the centrosome in many mammalian  
172 cell types (Masson and El Ghouzzi, 2022), we noted that in polarized MDCK monolayers the Golgi was not  
173 detected at the actin-clearing site around the apically docked basal body, but rather closer to the nucleus (Fig.  
174 S2B), so the basal-body localization of Rab19 appeared to be separate from its Golgi localization.

175 In Vps41 KO or CQ-treated MDCK cells, however, Rab19 localized strongly to the membranes of enlarged  
176 LE/Ls (Fig. 3C,D). Importantly, this was accompanied by a reduction in basal-body enrichment of Rab19 (Fig.  
177 3A,B). These results indicate that impairment of lysosomal fusion results in aberrant retention of Rab19 on LEs,  
178 thus, depleting the pool of Rab19 available to mediate actin clearing and ciliogenesis at the basal body. The portion  
179 of Rab19 localizing in the Golgi was also reduced in Vps41 KO or CQ-treated cells, although these conditions did  
180 not appear to grossly disrupt the structure of the Golgi itself (Fig. S2A,B), suggesting that the accumulation of  
181 Rab19 on LEs sequestered Rab19 away from its normal sites of action at both the basal body and the Golgi.

182 To assess whether depletion of Rab19 from the basal body was the mechanism for the actin-clearing and  
183 ciliogenesis defects in Vps41 KO and CQ-treated cells, we tested whether overexpression of Rab19 could rescue  
184 the defects. Indeed, GFP-Rab19 overexpression fully rescued actin clearing and ciliation in CQ-treated cells and  
185 partially rescued these phenotypes in Vps41 KO cells (Fig. 3E,F), and overexpression of GFP-Rab19 also  
186 enhanced ciliation in control cells (Fig. 3E,F), supporting the hypothesis that mislocalization of Rab19 contributes to  
187 the actin-clearing and ciliogenesis defects produced by inhibition of lysosomal fusion (either by Vps41-KO or by CQ  
188 treatment).

189

## 190 **Rab19 functions in cargo transport to LEs, and interacts with V-ATPase**

191 The observation that Rab19 accumulates on LEs in Vps41 KO or CQ-treated cells led us to investigate how Rab19  
192 is involved in the endolysosomal pathway. Since Rab19 showed little localization to LE/Ls at steady state but  
193 accumulated on LEs when their fusion was blocked (Fig. 3C,D), it is likely that under normal conditions Rab19 is  
194 transiently recruited to LE membranes and then released from those membranes following lysosomal fusion. To  
195 investigate the function of Rab19 targeting to LE/Ls, we examined the LE/L phenotypes for Rab19 KO and for the  
196 Rab19 constitutively active (CA) mutant Q79L in MDCK cells. Neither Rab19 KO nor Rab19-CA showed any major  
197 effect on LE/L size under steady-state conditions (Fig. S2C,D). However, Rab19-CA expression greatly  
198 exaggerated the enlarged LE/L phenotype induced by CQ (Fig. S2C,D). A likely interpretation for this finding is that  
199 Rab19 may mediate trafficking of certain cargoes to LE/Ls. Under conditions of normal lysosomal function, an  
200 altered rate of delivery of those cargoes may have limited effect on LE/L size because the cargo is rapidly degraded  
201 in lysosomes, and thus it is only when lysosomal degradation is inhibited (e.g. by CQ treatment) that increased  
202 delivery of certain cargoes results in increased swelling of the stalled LE/Ls.

203 Interestingly, the recruitment of Rab19 to LEs did not appear to rely on its binding to the HOPS complex,  
204 since it was observed in the Vps41 KO cells (Fig. 3C,D) in which HOPS complex formation is disrupted (Ostrowicz  
205 et al., 2010) and the remainder of HOPS does not localize to LEs (Fig. S2E). This suggests that Rab19 is targeted  
206 to the LE by some other factor (or alternatively Rab19 could be targeted to the EE and remain associated with the  
207 endosome as it matures to LE) and may subsequently interact with the HOPS complex on the LE membrane.  
208 Examining previously published proteomics analysis of Rab19 binding partners (Jewett et al., 2021) for factors  
209 relating to the endolysosomal pathway, we noted that in addition to the HOPS complex, Rab19 also interacted with  
210 several subunits of the cytosolic V1 sector of the vacuolar-type ATPase (V-ATPase). The V-ATPase is a proton  
211 pump which assembles on endolysosomal membranes to acidify these organelles (McGuire et al., 2017;  
212 Podinovskaia and Spang, 2018), and has also been shown to act as a pH sensor mediating recruitment of certain  
213 cytosolic trafficking factors to endosomal membranes in an manner dependent on the intra-endosomal pH  
214 (Hurtado-Lorenzo et al., 2006; Marshansky et al., 2014). In contrast to the GTP-dependent binding of Rab19 to  
215 HOPS, the proteomics results indicated that Rab19 binding to the V-ATPase subunit ATP6V1A was GTP-  
216 independent (Jewett et al., 2021), suggesting that ATP6V1A can interact with both GTP-bound (active and  
217 membrane-associated) and GDP-bound (inactive and cytosolic) forms of Rab19. Using GFP nanobody to pull-down  
218 GFP-Rab19 from MDCK cell lysate, we confirmed that Rab19 does interact with ATP6V1A in a GTP-independent  
219 manner (Fig. S2F). The V-ATPase could therefore be a plausible candidate to regulate the transient recruitment of  
220 Rab19 to LEs.

221

## 222 **Rab19 interacts with core subunits of both HOPS and CORVET complexes**

223 To explore the significance of the Rab19-HOPS interaction, we set out to identify which subunit of the HOPS  
224 complex mediates its binding to Rab19. The HOPS complex contains two HOPS-specific subunits (Vps41 and  
225 Vps39) along with four core subunits (Vps11, Vps16, Vps18, and Vps33A) which are shared with the early  
226 endosomal CORVET complex (Balderhaar and Ungermann, 2013) (Fig. 4A).

227 As previously reported (Jewett et al., 2021), glutathione bead pull-down experiments with recombinantly  
228 produced GST-Rab19 confirmed that Rab19 in its GTP-bound state interacts with HOPS (as determined by  
229 immunoblotting for the Vps11 subunit) in WT MDCK cell lysates (Fig. 4B and Fig. S3A). Importantly, we also

230 detected the interaction of Rab19 with Vps11 in Vps41 KO MDCK lysates (Fig. 4B and Fig. S3A), suggesting that  
231 Rab19 binding to HOPS complex is not mediated by Vps41. To probe the dependence of Rab19-HOPS interaction  
232 on the other HOPS subunits, we used siRNA to deplete each of the HOPS subunits in HEK293T cells (Fig. 4C,D,  
233 and Fig. S3B-E). Knockdown of any one of the four HOPS/CORVET core subunits severely disrupted the entire  
234 HOPS complex, as indicated by decreased levels of Vps11 and Vps41 in cell lysates (Fig. 4C and Fig. S3B,F), so  
235 the roles of these core subunits in Rab19-HOPS binding could not be individually assessed. Knockdown of Vps39,  
236 in contrast, had only moderate effects on Vps11 protein levels, and did not impair the interaction of Rab19 with  
237 Vps11 (Fig. 4C,D, and Fig. S3B-D,F). Thus, neither one of the HOPS-specific subunits, Vps41 or Vps39, appear to  
238 be required for Rab19-HOPS interaction.

239 The HOPS complex has been shown to bind Rab7 *via* both Vps41 and Vps39 (Brett et al., 2008; Bröcker et  
240 al., 2012). We wondered whether Rab19 might similarly interact with both Vps41 and Vps39, which could explain  
241 why knockdown of either Vps41 or Vps39 alone failed to disrupt the interaction. However, co-depletion of both  
242 Vps41 and Vps39 still did not reduce Rab19 binding to Vps11 (Fig. 4D and Fig. S3D). We further investigated  
243 whether Rab19 competes with Rab7 for binding to HOPS, by testing whether addition of purified recombinant Rab7  
244 in the GST-Rab19 pulldown experiment would reduce Rab19-HOPS binding. Addition of Rab7 did not impair  
245 Rab19-HOPS interaction (Fig. 4D and Fig. S3D,G), suggesting that Rab19 binds to HOPS at a different site than  
246 Rab7 does. All these results indicate that Rab19-HOPS interaction is independent of HOPS-specific subunits,  
247 suggesting that HOPS core subunits may mediate interaction with Rab19.

248 Since HOPS and CORVET share the same core subunits, we therefore wondered whether Rab19 also  
249 interacts with the CORVET complex. To test this possibility, we performed GST-Rab19 pull-down assays using  
250 lysates of HEK293T cells expressing CORVET-specific subunit Vps8-GFP. Vps8-GFP (presumably as part of  
251 CORVET complex) did bind to GST-Rab19 (Fig. 4E and Fig. S3H), supporting the hypothesis that Rab19 can also  
252 interact with CORVET. Collectively, these results suggest that Rab19 likely binds to HOPS/CORVET core subunits,  
253 and thus, likely interacts not only with HOPS but also with CORVET complex.

## 254 255 **EEs but not LE/Ls are found at the site of ciliogenesis**

256 If Rab19 binds to both HOPS and CORVET, we wondered whether either HOPS or CORVET are directly involved  
257 in the ciliogenesis function of Rab19. To test this question, we examined the subcellular localization of the  
258 HOPS/CORVET core by immunostaining for Vps11. Vps11 puncta were frequently observed at the periphery of the  
259 actin cortical clearing (Fig. 5A,B,D), where they sometimes overlapped with Rab19 (Fig. 5A), potentially supporting  
260 a direct role for HOPS and/or CORVET in ciliogenesis.

261 We were unable to directly assess the distinct localizations of HOPS and CORVET, because commercially  
262 available antibodies for the HOPS-specific and CORVET-specific subunits did not perform adequately for  
263 immunofluorescence in MDCK cells, and overexpression of tagged HOPS subunits disrupts the function of these  
264 complexes in ciliogenesis (unlike Rab19, for which overexpression of a tagged form enhances ciliation in WT cells  
265 and rescues ciliation in Rab19 KO, indicating that tagged Rab19 is functional in ciliogenesis) (Jewett et al., 2021).  
266 To distinguish whether the Vps11 detected at the site of ciliogenesis represented HOPS or CORVET, we therefore  
267 used immunostaining for early endosome antigen 1 (EEA1) as a marker for EEs (organelles containing CORVET),  
268 and LysoTracker dye as a marker for LE/Ls (organelles containing HOPS). EEA1, like Vps11, was often detected at  
269 the basal body and actin cortical clearing (Fig. 5B,F,G), and Vps11 colocalized strongly with EEA1, both at the

270 ciliation site and overall in the cells (Fig. 5B,C,H). In contrast, LysoTracker showed little localization to the site of  
271 ciliogenesis (Fig. 5D,F) and little colocalization with Vps11 (Fig. 5D,E,H). Thus, it appears that in WT MDCK the  
272 majority of Vps11, including the Vps11 present at the site of ciliogenesis, is part of CORVET complex on EEs, with  
273 relatively little Vps11 in HOPS complex on LE/Ls.

274 To probe whether EEs function in ciliogenesis or in subsequent trafficking to or from cilia, we also  
275 examined EEA1 localization with respect to Arl13b. EEA1-positive EEs were frequently found at sites of actin  
276 cortical clearing that did not show cilia, and also at the base of Arl13b-positive cilia (Fig. S4A), suggesting that  
277 these EEs may be involved both early in ciliogenesis and later in ciliary trafficking. We then wondered whether  
278 Rab19 and its interaction with CORVET was responsible for targeting EEs to the ciliogenesis site. Rab19 KO  
279 MDCK cells also showed EEA1 at the basal body (Fig. S4B), indicating that Rab19 is not required for localizing EEs  
280 to this site. It may instead be that Rab19 transports some ciliogenesis factors to the EEs at the basal body to  
281 promote ciliogenesis. We also tested whether EEs at the site of ciliogenesis were perturbed by inhibition of  
282 lysosomal fusion. EEA1 was observed at basal bodies in Vps41 KO and CQ-treated as well as WT MDCK (Fig.  
283 S4C), indicating that inhibition of lysosomal fusion did not disrupt the targeting of EEs to the site of ciliogenesis,  
284 although it might well be that the contents of these EEs are dysregulated by accumulation of cargoes that would  
285 normally be transported to lysosomes and degraded.

286 These observations support the idea that the interaction of CORVET with Rab19 might play a direct role in  
287 ciliogenesis, although further study will be needed to demonstrate that role. In contrast, we see little evidence for  
288 HOPS or LE/Ls at the site of ciliogenesis (albeit we cannot rule out the possibility that small LE/Ls with LysoTracker  
289 signal below the detection limit of this assay could be present there), suggesting that HOPS and its interaction with  
290 Rab19 are likely not directly involved in ciliogenesis. This is consistent with the model in which the ciliogenesis  
291 defects of Vps41 KO or CQ-treated cells are due to aberrant retention of Rab19 on LEs impeding recruitment of  
292 Rab19 to the site of ciliogenesis (Fig. 6).

293

## 294 **DISCUSSION**

295 In this study, we set out to elucidate the role of the HOPS tethering complex in apical actin cortical clearing and  
296 primary ciliogenesis. Knockout or mutation of HOPS subunits was recently shown to disrupt primary ciliogenesis  
297 and ciliary signaling (Breslow et al., 2018; Iaconis et al., 2020; Jewett et al., 2021). In polarized epithelial MDCK  
298 monolayers, Vps41 KO was shown to block a key early step of ciliogenesis in which the apical cortical actin is  
299 remodeled and cleared around the apically docked basal body to allow the ciliary axoneme to grow into the  
300 extracellular space (Hoffman and Prekeris, 2022; Jewett et al., 2021). The canonical role of the HOPS complex is  
301 as a membrane tether that mediates lysosomal fusion and is thus required for lysosomal degradation (Balderhaar  
302 and Ungermann, 2013; van der Beek et al., 2019). It was unclear whether the requirement for HOPS in ciliogenesis  
303 reflected a requirement for lysosomal trafficking in ciliogenesis, or whether it represented a separate function of the  
304 HOPS complex. It was also unknown whether HOPS participates directly in actin-clearing and ciliogenesis at the  
305 basal body, or whether its role is indirect. Addressing these outstanding questions is the main focus of this study.

306

### 307 **Requirement for lysosomal trafficking in ciliogenesis**

308 We reasoned that if the actin-clearing and ciliogenesis role of HOPS were a consequence of its role in  
309 lysosomal fusion, then treatment with CQ, a pharmacological inhibitor of lysosomal fusion (Mauthe et al., 2018;

310 Mullock et al., 1998), should recapitulate the actin-clearing and ciliogenesis defects of Vps41 KO. CQ had similar  
311 effects on LE/Ls in MDCK cells as Vps41 KO, producing enlarged LEs swollen with undegraded cargo (Fig. 1A,B).  
312 Actin clearing and ciliogenesis were blocked in CQ-treated cells as in Vps41 KO cells (Fig. 1C-G), suggesting that  
313 those phenotypes were indeed due to disruption of lysosomal fusion, rather than a separate non-lysosomal function  
314 of Vps41. In both Vps41 KO and CQ-treated cells, actin-clearing defects were accompanied by defects in exclusion  
315 of non-ciliary membrane proteins (Fig. 2A) and appeared to be upstream of ciliation defects (Fig. 2B-D),  
316 emphasizing the importance of the apical actin cortical clearing step for ciliogenesis in polarized epithelia.

317 These results align with some previous literature linking lysosomal fusion to ciliogenesis. For example, two  
318 inositol-5-phosphatases of which mutations cause cilia defects in patients (INPP5E, involved in Joubert Syndrome,  
319 and OCRL, involved in Lowe Syndrome) are important for autophagosome-lysosome fusion (De Leo et al., 2016;  
320 Hasegawa et al., 2016; Yamamoto and Mizushima, 2021). Depletion of VAMP7, a SNARE protein involved in  
321 lysosomal fusion, was also shown to disrupt ciliation in MDCK cells, although depletion of the lysosomal enzyme  $\alpha$ -  
322 gal A did not affect ciliation (Szalinski et al., 2014), which may suggest that it is specifically the fusion step of  
323 lysosomal trafficking, rather than lysosomal function overall, that is important to ciliogenesis.

324 While these reports, including the experiments shown here, demonstrate the requirement for lysosomal  
325 fusion during ciliogenesis, what remains unclear is the mechanism by which lysosomal fusion affects cilia formation.  
326 Recent literature suggested a potential reason why lysosomal fusion might be required for ciliogenesis: several  
327 studies have shown that certain ciliogenesis inhibitors, including OFD1 (Tang et al., 2013), MYH9 (Yamamoto et  
328 al., 2021), and CP110 (Liu et al., 2021), are degraded by selective autophagy to promote ciliogenesis. Since  
329 autophagy involves HOPS-dependent autophagosome-lysosome fusion (Jiang et al., 2014), we hypothesized that  
330 the ciliogenesis defects of Vps41 KO MDCK cells might be due to a failure to degrade these ciliogenesis inhibitors.  
331 However, although autophagy was impaired in Vps41 KO cells (Fig. S1A,B), these cells did not show excess  
332 accumulation of MYH9 (Fig. S1C-E), OFD1, or CP110 (Fig. S1D,E). We also did not observe MYH9 accumulation  
333 upon treatment with autophagy inhibitor BafA (Fig. S1C), suggesting that MYH9 was not an autophagy cargo in  
334 polarized MDCK cells. The difference between these results and those of previous studies (Liu et al., 2021; Tang et  
335 al., 2013; Yamamoto et al., 2021) may reflect differences between starvation-induced and starvation-independent  
336 ciliogenesis. Serum starvation is commonly used to induce ciliogenesis in cultured cells, especially in non-polarized  
337 cells that use an intracellular ciliogenesis pathway. However, serum starvation also induces autophagy, and it was  
338 under starvation conditions that autophagy of MYH9, OFD1, and CP110 was shown to be important for ciliogenesis  
339 (Liu et al., 2021; Pierce and Nachury, 2013; Tang et al., 2013; Yamamoto et al., 2021). In contrast, our study  
340 examined ciliogenesis in polarized MDCK monolayers that use an extracellular ciliogenesis pathway and do not  
341 require starvation. Thus, selective autophagy of ciliogenesis inhibitors may be required for starvation-induced  
342 ciliogenesis in some cell types, but not for ciliogenesis in polarized epithelial cells.

### 343 344 **Inhibition of lysosomal fusion disrupts recruitment of Rab19 to the site of ciliogenesis**

345 In searching for alternate explanations for the actin-clearing and ciliogenesis defects of Vps41 KO MDCK,  
346 we investigated Rab19, since previous work had shown that Rab19 drives actin-clearing during ciliogenesis and  
347 that the HOPS complex is a Rab19 effector (Jewett et al., 2021). As previously reported (Jewett et al., 2021), in WT  
348 MDCK monolayers, Rab19 localized to the actin cortical clearing around the basal body and only occasionally  
349 localized to LE/Ls (Fig. 3A-D). Rab19 was also observed in the Golgi apparatus (Fig. S2A,B), suggesting that the

350 role of Rab19 in ciliogenesis might involve transporting some ciliogenesis factors from the Golgi to the basal body.  
351 In Vps41 KO or CQ-treated cells, however, Rab19 accumulated on membranes of enlarged LEs and its recruitment  
352 to the basal body and Golgi was reduced (Fig. 3A-D and Fig. S2A,B).

353 In support of a hypothesis that depletion of Rab19 from the site of ciliogenesis contributes to the actin-  
354 clearing and ciliogenesis defects of Vps41 KO and CQ-treated cells, we found that GFP-Rab19 overexpression  
355 rescued those defects (Fig. 3E,F). Thus, retention of Rab19 on LEs in Vps41 KO and CQ-treated cells reduces the  
356 fraction of cellular Rab19 that can be recruited to the basal body, thereby disrupting actin-clearing and ciliogenesis  
357 (Fig. 6). Interestingly, GFP-Rab19 overexpression only partially rescues ciliation in Vps41 KO cells, while fully  
358 rescuing the phenotype in CQ-treated cells (Fig. 3E,F), suggesting that in Vps41 KO cells a reduction of Rab19 at  
359 the basal body contributes to but is not the sole reason for ciliation defects. It may be that HOPS complex depletion  
360 also affects the localization of other, as yet unidentified, ciliogenesis regulators.

361

### 362 **Rab19 function at LEs**

363 Besides revealing a mechanism by which actin-clearing and ciliogenesis was disrupted in HOPS-depleted cells, the  
364 observation that Rab19 accumulates on LEs when lysosomal fusion is inhibited (Fig. 3C,D) also suggested that  
365 Rab19 may have a previously uncharacterized function at the LE. Rab19 KO did not affect LE/L size, but  
366 expression of the Rab19-CA mutant exacerbated the enlargement of LEs upon CQ treatment (Fig. S2C,D). One  
367 potential explanation is that Rab19 may mediate the transport of certain cargoes to LEs, which under normal  
368 conditions constitute only a minor fraction of total LE cargo volume, but when downstream lysosomal degradation is  
369 blocked then an increase in delivery of these Rab19 cargoes results in increased swelling of the LEs. Further  
370 studies will be needed to identify these Rab19-dependent LE cargoes. Rab19 was previously reported to localize to  
371 the Golgi and trans-Golgi network (TGN) in *Drosophila* (Sinka et al., 2008), and we confirmed that Rab19 is also  
372 found in the Golgi in MDCK cells (Fig. S2A,B), so it may be that Rab19 mediates a TGN-to-LE/L transport route.  
373 The HOPS complex is involved in TGN-to-LE/L transport of certain lysosomal membrane proteins via the AP-3  
374 pathway (Balderhaar and Ungermann, 2013; Schoppe et al., 2020), and proteomics for Rab19 binding partners  
375 suggest Rab19 may also interact with the AP-3 complex (Jewett et al., 2021). This raises an interesting possibility,  
376 which remains to be tested by future studies, that Rab19-HOPS interaction could be involved in AP-3-dependent  
377 TGN-to-LE/L transport. We furthermore found that Rab19 interacts with V-ATPase (Fig. S2F). Since V-ATPase can  
378 act as a pH sensor to recruit trafficking factors to endo/lysosomes in an acidification-dependent manner (Hurtado-  
379 Lorenzo et al., 2006), this interaction could potentially be involved in targeting Rab19 to the LE or in releasing  
380 Rab19 from the lysosome following lysosomal fusion.

381

### 382 **Differential roles of LE/L-associated HOPS complex and EE-associated CORVET complex in ciliogenesis**

383 HOPS is a large protein complex that was shown to bind to other Rab GTPases, specifically to Rab7 which  
384 interacts with the HOPS-specific subunits, Vps41 and Vps39. We investigated the interaction between Rab19 and  
385 HOPS, aiming to determine which of the HOPS subunits was responsible for binding Rab19. Surprisingly, we found  
386 that this interaction was independent of Vps41 and Vps39 and appeared instead to be mediated by the core  
387 complex (Vps11, Vps16, Vps18, and Vps33A) that is shared between LE/L-associated HOPS and EE-associated  
388 CORVET (Fig. 4 and Fig. S3). Importantly, this revealed that Rab19 may interact with CORVET on EEs as well as  
389 with HOPS on LE/Ls. This led us to probe the respective roles of EEs and LE/Ls in ciliogenesis.

390 The original work that identified HOPS as being required for ciliogenesis (Jewett et al., 2021) left open the  
391 question of whether HOPS is actually localized to the basal body to participate directly in ciliogenesis. To address  
392 the question of HOPS localization, we first used immunostaining for the HOPS/CORVET core subunit Vps11 and  
393 found that Vps11-positive vesicles were frequently present at the basal body (Fig. 5A,B,D). To determine whether  
394 the Vps11 at the basal body was part of the LE/L-associated HOPS complex or part of the EE-associated CORVET  
395 complex, we used LysoTracker as a marker for LE/Ls and EEA1 immunostaining as a marker for EEs. EEA1-  
396 positive EEs were often observed at the basal body and actin clearing, while LysoTracker-positive LE/Ls were not  
397 (Fig. 5B,D,F,G). Thus, it appears that the CORVET rather than HOPS is present at the site of ciliogenesis. A role  
398 for EEs at the basal body is consistent with previous studies which observed EEA1-positive or Rab5-positive EEs at  
399 the base of cilia in various cell types including RPE1 cells, fibroblast-like synoviocytes, astrocytes, and *C. Elegans*  
400 sensory neurons (Blacque et al., 2018; Hu et al., 2007; Leitch et al., 2014; Moser et al., 2009; Rattner et al., 2010).  
401 This has been interpreted as representing a zone of endocytosis around the base of the cilium, which in these cell  
402 types is embedded in a membrane invagination termed the “ciliary pocket” (Molla-Herman et al., 2010; Moser et al.,  
403 2009; Rattner et al., 2010). Cilia of polarized epithelial cells, such as the MDCK cells in this study, have been  
404 described as protruding directly from the plasma membrane without a ciliary pocket (Ghossoub et al., 2011; Molla-  
405 Herman et al., 2010). However, our observations may indicate that these cell types nonetheless have a comparable  
406 endocytosis domain around the base of the cilium. It remains unclear whether these EEs are required for  
407 ciliogenesis, with some studies finding that ciliation is not impaired by mutations of the EE regulator Rab5 or other  
408 early endocytic machinery (Blacque et al., 2018). There is, however, evidence that endocytic trafficking at the base  
409 of cilia regulates ciliary membrane receptor localization and signaling functions (Blacque et al., 2018; Clement et  
410 al., 2013); we would speculate that such may be the role of the CORVET-containing EEs at the basal body in  
411 MDCK cells.

412

### 413 **Conclusions and biomedical implications**

414 Collectively, our observations favor a model in which the HOPS complex is not directly involved in  
415 ciliogenesis at the basal body (Fig. 6). Instead, HOPS-mediated lysosomal fusion occurring elsewhere in the cell  
416 maintains the flow of endolysosomal trafficking, which is needed to balance Rab19 activity between the separate  
417 functions of Rab19 in ciliogenesis and in LE cargo transport. Under normal conditions, a fraction of Rab19 is  
418 transiently recruited to LEs and then cycles off of these membranes after lysosomal fusion, keeping a large pool of  
419 Rab19 available to drive actin-clearing and ciliogenesis at the basal body (Fig. 6A). When lysosomal fusion is  
420 impaired, as in Vps41 KO or CQ-treated cells, then Rab19 is abnormally retained on LEs which fail to fuse to  
421 lysosomes; this depletes the pool of Rab19 available to be recruited to the basal body, and thereby disrupts Rab19-  
422 mediated actin-clearing and ciliogenesis (Fig. 6B).

423 These results highlight a relatively unexplored way that defects in lysosomal trafficking can disrupt other  
424 cellular processes such as ciliogenesis: besides blocking the degradation of lysosomal cargoes, such defects also  
425 dysregulate the activity of cellular machinery that is normally shared between endolysosomal functions and other  
426 functions. While we focused here on the mislocalization of Rab19 and its effect on ciliogenesis, it would be  
427 interesting for future studies to investigate what other factors are abnormally retained on LE/Ls when their fusion is  
428 impaired and what other cellular functions may be dysregulated thereby.

429 This mechanism may be relevant to certain ciliopathies and other medical conditions involving defects in  
430 lysosomal fusion machinery. As mentioned above, these include Joubert Syndrome caused by INPP5E mutation  
431 and Lowe Syndrome caused by OCRL mutation (De Leo et al., 2016; Hasegawa et al., 2016); both of these genetic  
432 disorders manifest with ciliary defects and the causative genes are important for lysosomal fusion. For mutations in  
433 Vps41 and other HOPS subunits, the main disease manifestations are neurological disorders often involving  
434 dystonia (Monfrini et al., 2021a; Monfrini et al., 2021b; Sanderson et al., 2021; Steel et al., 2020; van der Welle et  
435 al., 2021). These HOPS mutations cause lysosomal abnormalities in fibroblasts (Monfrini et al., 2021a; Steel et al.,  
436 2020; van der Welle et al., 2021), but the mechanism linking those lysosomal defects to the dystonia phenotype is  
437 unclear. Investigating whether Rab19 is mislocalized and whether cilia are impaired by these HOPS mutations  
438 could inform potential treatments for HOPS-associated neurological disorders. Besides genetic diseases, other  
439 conditions can also impair lysosomal fusion and thus might impact cilia by the mechanism outlined here. For  
440 example, CQ and the related drug hydroxychloroquine (HCQ), which similarly inhibits autophagosome-lysosome  
441 fusion (Mondal et al., 2022), are used to treat malaria and certain autoimmune diseases; these drugs can cause  
442 adverse effects including neuropsychiatric events, cardiotoxicity, and retinopathy (Doyno et al., 2021;  
443 Schrezenmeier and Dörner, 2020). In light of our results showing that CQ blocks ciliogenesis, it will be important to  
444 assess whether cilia are altered in patients treated with CQ or HCQ, since cilia dysfunction could contribute to  
445 adverse effects of these drugs. Thus, the indirect role of lysosomal fusion in regulating Rab19 activity for  
446 ciliogenesis is potentially relevant to a variety of diseases ranging from genetic disorders to malaria.

447

## 448 **MATERIALS AND METHODS**

### 449 **Cell lines and cell culture**

450 All of the experiments, except where otherwise noted, were performed in polarized epithelial Madin Darby canine  
451 kidney cells (MDCK.2; #CRL-2936, ATCC, Manassas, VA, USA). The human embryonic kidney epithelial-like  
452 HEK293T cell line (#CRL-3216, ATCC) was used for the siRNA and Vps8-GFP experiments, and for lentiviral  
453 vector production to generate stable MDCK cell lines by lentiviral transduction. Cells were maintained at 37°C with  
454 5% CO<sub>2</sub> in complete media consisting of DMEM (#10-017-CV, Corning, Corning, NY, USA) with 10% FBS (#PS-  
455 300, Phoenix Scientific, San Marcos, CA, USA) and 1x penicillin-streptomycin (#30-002-CL, Corning).

456 The generation of a parental MDCK line stably expressing Tet-inducible Cas9, and the generation of the  
457 Vps41 and Rab19 CRISPR KO lines on that background, was previously described (Jewett et al., 2021). The  
458 control cell line referred to as “WT MDCK” throughout the manuscript is the Tet-inducible Cas9 parental line, to  
459 provide an appropriately matched control for the CRISPR knockout lines. The cell lines labeled as Vps41 KO#1 and  
460 Vps41 KO#2 are two clonal lines of Vps41 KO MDCK. The MDCK cell lines stably overexpressing GFP-Rab19 on  
461 the WT or Rab19 KO background were previously described (Jewett et al., 2021). The MDCK cell lines stably  
462 overexpressing GFP-Rab19 on the Vps41 KO background, and GFP-MYH9 on the WT or Vps41 KO background,  
463 were generated by the same approach, using lentiviral transduction and puromycin selection.

464 For experiments with CQ, the cells were treated with 10 μM chloroquine diphosphate salt (#200-055-2,  
465 Sigma, St. Louis, MO, USA) in the media, beginning approximately 0.5-2 hours after seeding the cells for the  
466 experiment, and refreshed daily. The experiments with BafA in Fig. S1 used 100 nM bafilomycin A1 (#S1413,

467 Selleck Chemicals, Houston, TX, USA) in the media for the final 16 hrs. For the serum-starved conditions in Fig.  
468 S1A, complete media was replaced with serum-free DMEM for 48 hours.

#### 469 **Plasmids**

470 The pLVX-GFP-Rab19 lentiviral transfer plasmid used to establish the GFP-Rab19 stable cell lines was previously  
471 described (Jewett et al., 2021). A pLVX-GFP-MYH9 transfer plasmid was cloned by ligating a NdeI/Sall-digested  
472 GFP-MYH9 cassette from CMV-GFP-NMHC II-A (gift from Robert Adelstein, Addgene plasmid #11347) into  
473 NdeI/XhoI-digested pLVX-Puro vector. For lentiviral vector production, the transfer plasmid was co-transfected with  
474 the packaging plasmid p $\Delta$ 8.9 and pseudotyping plasmid pVSV-G into HEK293T cells.

475 The pGEX-KG-Rab19 plasmid, encoding GST-tagged Rab19 for expression in *E. coli* for recombinant  
476 protein production, was previously described (Jewett et al., 2021).

#### 477 **Antibodies and dyes**

478 *Table 1: Antibodies and fluorescence dyes used for immunofluorescence and western blotting.*

<b>Primary antibodies</b>	Source	Product number	Application
$\gamma$ -Tubulin	Sigma-Aldrich	#T5326	IF
Acetyl- $\alpha$ -Tubulin	Cell Signaling Technology (Danvers, MA, USA)	#5335	IF
Arl13b	Antibodies Inc (Davis, CA, USA)	#73-287	IF
LC3B	Novus Bio (Centennial, CO, USA)	#NB600-1384	WB and IF
MYH9	Sigma-Aldrich	#M8064	WB
OFD1	Abcam (Waltham, MA, USA)	#ab222837	WB
CP110	ProteinTech (Rosemont, IL, USA)	#12780-1-AP	WB
GM130	BD Biosciences (San Jose, CA, USA)	#610822	IF
Vps11	Santa Cruz Biotechnology (Dallas, TX, USA)	#sc-515094	WB and IF
Vps41	Santa Cruz Biotechnology	#sc-377271	WB
ATP6V1A	Novus Bio	#NBP2-55148	WB
$\beta$ -tubulin	LI-COR (Lincoln, NE, USA)	#926-42211	WB
$\alpha$ -Tubulin	Sigma-Aldrich	#T6074	WB
$\alpha$ -Tubulin	Santa Cruz Biotechnology	#sc-23948	WB
GFP	Thermo Fisher Scientific (Waltham, MA, USA)	#A11122	WB
<b>Secondary antibodies</b>	Source	Product number	Application

AF488 anti-mouse	Jackson ImmunoResearch (West Grove, PA, USA)	#715-545-150	IF
AF594 anti-mouse	Jackson ImmunoResearch	#715-585-150	IF
AF488 anti-rabbit	Jackson ImmunoResearch	#711-545-152	IF
AF594 anti-rabbit	Jackson ImmunoResearch	#711-585-152	IF
AF647 anti-rabbit	Thermo Fisher Scientific	#A-21245	IF
AF488 anti-Mouse IgG2a	Thermo Fisher Scientific	#A-21131	IF
AF568 anti-Mouse IgG1	Thermo Fisher Scientific	#A-21124	IF
IRDye 680RD anti-mouse	LI-COR	#926-68072	WB
IRDye 800CW anti-rabbit	LI-COR	#926-32213	WB
<b>Dyes</b>	<b>Source</b>	<b>Product number</b>	<b>Application</b>
LysoTracker Red DND-99	Thermo Fisher Scientific	#L7528	IF
Hoechst	AnaSpec (Fremont, CA, USA)	#AS-83218	IF
Phalloidin AF647	Thermo Fisher Scientific	#A22287	IF

479

## 480 **Western blotting**

481 For western blotting of cell lysates, MDCK samples cultured at high confluency were washed with phosphate  
482 buffered saline (PBS) and lysed in a buffer of Tris buffered saline (TBS) with 1% Triton X-100 and 1 mM EDTA for  
483 30 min on ice, then centrifuged for 20 min at 15,000Xg at 4°C. The supernatants of the cell lysates were  
484 normalized for total protein concentration according to Bradford assay (#5000006, Bio-Rad, Hercules, CA, USA),  
485 mixed with SDS loading dye, and boiled for 5-10 min at 95°C. The samples were then run on SDS-PAGE,  
486 transferred to PVDF membranes, blocked for at least 20 min in a buffer consisting of Intercept (TBS) Blocking  
487 Buffer (#927-60001, LI-COR) diluted 1:3 in TBS with 0.05% Tween-20 (TBST), probed with the primary antibodies  
488 diluted in blocking buffer for at least 2 hours at room temp or overnight at 4°C, washed 4x ≥5 min with TBST,  
489 probed with the secondary antibodies diluted in blocking buffer for 1-2 hours at room temp, washed 4x ≥5 min with  
490 TBST and once with TBS, and then imaged on an Odyssey DLx imaging system (LI-COR).

491 Densitometry of the blot images was performed in Image Studio Lite Version 5.2.5 (LI-COR) using median  
492 background subtraction. Detected levels of the target protein were normalized according to a tubulin loading  
493 control, then normalized to the level in detected in the WT MDCK control in the given experiment.

## 494 **GST-Rab19 pull-down assays**

495 GST-tagged Rab19 protein was recombinantly produced in BL21 Codon Plus *E. coli*, purified using glutathione  
496 agarose beads and eluted with free glutathione as previously described (Jewett et al., 2021), and used for  
497 glutathione bead pull-down assays with cell lysates, as previously described (Jewett et al., 2021; Willenborg et al.,  
498 2011). The bead eluates and cell lysates were then analyzed by SDS-PAGE and western blotting as described  
499 above.

#### 500 **siRNA knockdowns of HOPS subunits**

501 The siRNAs (listed below) were purchased from Qiagen (Germantown, MD, USA) and were transfected into  
502 HEK293T cells using Lipofectamine RNAiMAX transfection reagent (#13778075, Thermo Fisher Scientific), and  
503 samples were harvested 2 days post transfection. For RT-qPCR validation of the siRNA knockdowns, RNA was  
504 isolated using TRIzol reagent (#15596026, Thermo Fisher Scientific), cDNA was synthesized using the SuperScript  
505 IV First-Strand Synthesis System (#18091050, Thermo Fisher Scientific), and qPCR was performed using iTaq  
506 Universal SYBR Green Supermix (#1725121, Bio-Rad), with primers (listed below; purchased from Integrated DNA  
507 Technologies, Coralville, IA, USA) designed to span an exon-exon junction to prevent amplification from genomic  
508 DNA, and analyzed using a StepOnePlus Real-Time PCR machine (#4376600, Thermo Fisher Scientific). GAPDH  
509 was analyzed as a housekeeping gene control.

510 *Table 2: siRNAs and qPCR primers*

<b>siRNAs (Qiagen)</b>	Product number
Hs_VPS39_1	#SI00110271
Hs_VPS11_6	#SI02778167
Hs_VPS18_3	#SI00760501
Hs_VPS33A_6	#SI03229436
Hs_VPS16_5	#SI03024483
Hs_VPS41_4	#SI00105665
<b>qPCR primers (IDT)</b>	Oligo sequence
qPCR-Vps39-F	AGCTGCCTCTGCAAATCGAC
qPCR-Vps39-R	ACATCTGCTGGCACAACGTC
qPCR-Vps18-F	GACTTCACCCCTTCCGAGC
qPCR-Vps18-R	TGCCCAAGTCAATGCGGAG
qPCR-Vps16-F	ACCCGAGAGCATCCAGTTTG
qPCR-Vps16-R	CCTCATGCAGGAACCTCGTGG
qPCR-Vps33A-F	AAGGATCTGGGTGTCTTGGA
qPCR-Vps33A-R	CCCTCCAGGTAGCACTCTTTGA
qPCR-GAPDH-F	TAAAAGCAGCCCTGGTGAC
qPCR-GAPDH-R	CTCTGCTCCTCCTGTTTCGAC

511

## 512 **GFP-Rab19 pull-down assay**

513 MDCK cells expressing GFP-Rab19 on the Rab19 KO background were lysed and incubated with GST-tagged anti-  
514 GFP nanobody (recombinantly produced from pGEX6P1-GFP-Nanobody, Addgene Plasmid #61838) or with free  
515 GST for negative control, followed by GTP $\gamma$ S or GDP loading and GST pulldown as previously described (Jewett et  
516 al., 2021), and the IP eluates were analyzed by western blotting for ATP6V1A.

## 517 **Immunofluorescence experiments**

### 518 *Culturing of MDCK monolayers on transwell filters*

519 0.4  $\mu$ m pore PET membrane transwell filter inserts (12-well filters, #665640, Greiner Bio-One, Monroe, NC, USA; or  
520 24-well filters, #662640, Greiner Bio-One) in wells of tissue-culture well plates were pre-coated with rat-tail collagen  
521 and cured under UV light for  $\geq$ 30 min prior to use. MDCK cells were plated on the filters at a highly confluent  
522 density of approximately  $2.2 \times 10^5$  cells/cm $^2$  ( $2.5 \times 10^5$  cells per 12-well filter, or  $7.4 \times 10^4$  cells per 24-well filter). The  
523 cells were cultured on the filters, in complete media which was changed daily, for 3 days prior to fixation for  
524 experiments assessing ciliation, actin cortical clearing, and basal body localization phenotypes; or 2 days for some  
525 of the other experiments such as those assessing LE/L phenotypes. For experiments with LysoTracker, the live  
526 cells were stained with LysoTracker Red DND-99 (#L7528, Thermo Fisher Scientific) at 500 nM (1:2000 dilution) in  
527 complete media for the final 30 min prior to fixation.

### 528 *Immunostaining and confocal fluorescence microscopy*

529 The following immunostaining protocol was performed at room temp. Cells on transwell filters in well plates were  
530 fixed with 4% paraformaldehyde (#15710, Electron Microscopy Sciences, Hatfield, PA, USA) in PBS for 20 min,  
531 quenched 2X 5 min with 0.1 M glycine in PBS, and rinsed with PBS. The filters were then cut out of the transwell  
532 inserts and placed on parafilm in a humidified dish for the following steps. Filters were rinsed with PBS with 0.1%  
533 Triton X-100 (PBST), blocked with 10% normal donkey serum (#017-000-121, Jackson ImmunoResearch) in PBST  
534 for  $\geq$ 1 hr, and stained overnight with primary antibodies (listed above) diluted in blocking buffer. The next day, the  
535 filters were washed 5X  $\geq$ 5 min with PBST, stained with Hoechst and dye-labeled secondary antibodies (listed  
536 above) and/or Phalloidin for 2 hrs, washed 5X  $\geq$ 5 min with PBST and once with PBS, then mounted on slides  
537 (#TNR WHT90, Tanner Scientific, Sarasota, FL, USA) with Vectashield (#H-1000, Vector Laboratories, Newark,  
538 CA), covered with coverslips (#48366-067, VWR, Radnor, PA, USA) and sealed with clear nail polish. Confocal  
539 fluorescence microscopy images were acquired either on a Nikon A1R confocal microscope (Nikon, Tokyo, Japan)  
540 using a 60x oil objective and NIS-Elements AR software (Nikon), or on a Leica SP8 confocal microscope (Leica  
541 Microsystems, Wetzlar, Germany) using a 63x oil objective and LAS X software (Leica).

542 **Quantitative image analysis**

543 *LysoTracker compartments (LE/L) size analysis*

544 Z-stack images of MDCK monolayers (grown for 2 days on filters, and stained with LysoTracker) were acquired on  
545 the Nikon A1R confocal microscope, with 0.21  $\mu\text{m}$  pixel size and z-step. Analysis of LE/L size was performed in FIJI  
546 (Schindelin et al., 2012), as follows: 50  $\mu\text{m}$   $\times$  50  $\mu\text{m}$  ROIs were cropped from the LysoTracker Red channel image  
547 stack. The image stack was smoothed, a maximum intensity projection was taken, and rolling-ball background  
548 subtraction was applied with a radius of 20 pixels. The image was then binarized using the Yen thresholding  
549 algorithm. Particle analysis was applied to quantify the size of LysoTracker compartments, analyzing particles with  
550 size  $\geq 3$  pixels and circularity 0.50-1 and excluding those on edges. Between 6-8 technical replicates (ROIs) were  
551 averaged from each biological replicate for each condition. Outlier biological replicates were excluded (ROUT,  
552  $Q=2\%$ ).

553 *Measuring apical cortical actin clearing*

554 Z-stack images of MDCK monolayers (grown for 3 days on filters, and stained with anti- $\gamma$ -tubulin antibody and  
555 Phalloidin) were acquired on the Nikon A1R confocal microscope, with 0.28  $\mu\text{m}$  pixel size and z-step. Analysis of  
556 apical actin cortical clearing was performed in FIJI, as follows: The z-stack was resliced to obtain the side view.  
557 Individual basal bodies (marked by  $\gamma$ -tubulin) docked at the apical actin cortex (marked by Phalloidin) were selected  
558 for analysis. An 8  $\mu\text{m}$  wide  $\times$  5  $\mu\text{m}$  high ROI was drawn centered around the selected basal body. The Plot Profile  
559 function was used to measure the vertically averaged pixel intensities in the  $\gamma$ -tubulin and Phalloidin channels along  
560 the horizontal distance through the ROI. Each intensity profile was normalized to have mean=1, by dividing each  
561 intensity value by the mean of that entire profile. To determine the fraction of cortical actin remaining over the basal  
562 body, the mean of the values in the actin intensity profile within 0.3  $\mu\text{m}$  horizontal distance from the center of the  
563 ROI was divided by the mean of the values in the actin intensity profile between 2-4  $\mu\text{m}$  from the center of the ROI.  
564 Between 10-15 technical replicates (individual basal bodies) were averaged from each biological replicate for each  
565 condition.

566 *Measuring ciliation in MDCK cells*

567 Z-stack images of MDCK monolayers (grown for 3 days on filters, and stained with anti-Arl13b antibody and  
568 Hoechst) were acquired on the Nikon A1R confocal microscope, with 0.28  $\mu\text{m}$  pixel size and z-step. Analysis of the  
569 percentage of cells exhibiting an Arl13b-positive primary cilium was performed in FIJI, as follows: To count cilia, a

570 maximum intensity projection of the Arl13b channel stack was taken, and rolling-ball background subtraction was  
571 applied with a radius of 100 pixels. The image was binarized using the Shanbhag thresholding algorithm, and  
572 particle analysis was applied to quantify the number of Arl13b puncta, analyzing particles with size  $\geq 2$  pixels. To  
573 count cells, a maximum intensity projection of the Hoechst channel stack was taken, the image was smoothed, and  
574 rolling-ball background subtraction was applied with a radius of 100 pixels. The image was binarized using the  
575 MinError(I) thresholding algorithm, and watershed separation was used to distinguish overlapping nuclei. Particle  
576 analysis was applied to quantify the number of nuclei, analyzing particles with size  $\geq 150$  pixels. The number of cilia  
577 was then divided by the number of nuclei to calculate the percent ciliation. 3-4 technical replicates ( $142 \mu\text{m} \times 142$   
578  $\mu\text{m}$  fields of view) were averaged from each biological replicate for each condition.

#### 579 *Quantifying Rab19 enrichment at the basal body*

580 Z-stack images of GFP-Rab19-expressing MDCK monolayers (grown for 3 days on filters, and stained with anti- $\gamma$ -  
581 tubulin antibody and Phalloidin) were acquired on the Leica SP8 confocal microscope, with  $0.12 \mu\text{m}$  pixel size and  
582 z-step, spanning from above the apical cortex to a mid-basolateral plane of the monolayer. Analysis of the  
583 enrichment of Rab19 vesicles at the basal body was performed in FIJI, as follows: The z-stack was resliced to  
584 obtain the side view. Rolling ball background subtraction was applied with a radius of 75 pixels. Side view slices  
585 showing apically docked basal bodies were selected for analysis, and GFP-Rab19 signal in the image slice was  
586 binarized using the Yen thresholding algorithm. The binarized result was visually inspected to check that it was a  
587 reasonable representation of the Rab19 compartments in the original image. Any cells for which almost all pixels  
588 were thresholded as either uniformly positive or uniformly negative (which could occur when GFP-Rab19  
589 expression in the cell of interest was far brighter or far dimmer than in the other cells in the slice) were excluded  
590 from analysis. A “basal body” ROI of  $3 \mu\text{m} \times 2 \mu\text{m}$  was then drawn with its upper edge centered at the apical end of  
591 the basal body, and a “cytosol” ROI was drawn freehand to enclose all of the cytosol of the selected cell that was  
592 visible in the image slice, bounded by the Phalloidin-stained actin cortex and excluding the nucleus. The density of  
593 Rab19-positive pixels (number of positive pixels divided by total pixel area of the ROI) in the basal body ROI was  
594 divided by the density of Rab19-positive pixels in the cytosol ROI to obtain a measure of Rab19 enrichment at the

595 basal body. 10 technical replicates (individual cells) were averaged from each biological replicate for each  
596 condition.

#### 597 *Analyzing Rab19 colocalization with LysoTracker*

598 Z-stack images of GFP-Rab19-expressing MDCK monolayers (grown for 2 days on filters, and stained with  
599 LysoTracker) were acquired on the Leica SP8 confocal microscope, with 0.12  $\mu\text{m}$  pixel size. Background  
600 subtraction and binarization of the GFP-Rab19 and LysoTracker image channels was performed in FIJI, as follows:  
601 Rolling ball background subtraction was applied with a radius of 100 pixels. 30  $\mu\text{m}$  X 30  $\mu\text{m}$  ROIs were cropped  
602 from the image stack, and a single slice at a mid-apical level of the monolayer was selected for analysis. The image  
603 slice was binarized using the Yen thresholding algorithm. The fractional overlap (Manders' Colocalization  
604 Coefficients) (Manders et al., 1993) between GFP-Rab19 and LysoTracker was then computed using a custom  
605 script written in MATLAB (MathWorks, Natick, MA, USA). 4 technical replicates (ROIs) were averaged from each  
606 biological replicate for each condition.

#### 607 *Quantifying EEA1 and LysoTracker enrichment at the basal body*

608 Z-stack images of MDCK monolayers (grown for 3 days on filters, and stained with anti- $\alpha$ -tubulin antibody and anti-  
609 EEA1 antibody and/or LysoTracker) were acquired on the Leica SP8 confocal microscope, with 0.12  $\mu\text{m}$  pixel size  
610 and z-step, spanning from above the apical cortex to a mid-basolateral plane of the monolayer. Analysis of the  
611 enrichment of EEA1 and/or LysoTracker vesicles at the basal body was performed by the same method as  
612 described above for analysis of Rab19 enrichment at the basal body. 15 technical replicates (individual cells) were  
613 averaged from each biological replicate for each condition.

#### 614 *Analyzing Vps11 colocalization with EEA1 and with LysoTracker*

615 Z-stack images of MDCK monolayers (grown for 3 days on filters, and stained with Vps11 antibody and either  
616 EEA1 antibody or LysoTracker) were acquired on the Leica SP8 confocal microscope, with 0.12  $\mu\text{m}$  pixel size.  
617 Background subtraction and binarization, followed by computation of the fractional overlap in a selected z-slice at a  
618 mid-apical level of the monolayer, was performed by the same methods as described for Rab19/LysoTracker  
619 colocalization above.

#### 620 **Statistical analysis**

621 GraphPad Prism 9.5.0 software (GraphPad Software, Boston, MA, USA) was used to generate graphs and to  
622 calculate P-values. For all of the quantitative image analysis experiments, each data point on the graphs in the  
623 figures represents the mean of the technical replicates (ROIs or individual cells) for one biological replicate  
624 (separate experiment), except as noted for the graph in Fig. 2B where the data points represent individual technical  
625 replicates. P-values were calculated from the means for the biological replicates. For the analysis of percent  
626 ciliation, statistical significance was assessed by mixed-effects analysis with Geisser-Greenhouse correction and  
627 Šidák's multiple comparisons test. For the analysis of basal-body enrichment of EEA1 and LysoTracker, statistical  
628 significance was assessed by Kolmogorov-Smirnov test. For the other quantitative image analysis experiments,

629 statistical significance was assessed by Brown-Forsythe and Welch ANOVA test and Dunnett's T3 multiple  
630 comparisons test. For the western blot densitometry results, each data point on the graphs represents the result  
631 from one biological replicate (separate set of cell lysates), normalized to the loading control and then to the WT  
632 level of the target protein from the same biological replicate, and statistical significance was assessed by one-  
633 sample t-test.

634

#### 635 **ACKNOWLEDGEMENTS**

636 We thank Dr. Robert Adelstein for the gift of the CMV-GFP-NMHC II-A plasmid (Addgene #11347).

637 This work was funded by NIDDK grant #2R01DK064380-15 to R.P.

638 **REFERENCES**

- 639 **Anvarian, Z., Mykytyn, K., Mukhopadhyay, S., Pedersen, L. B. and Christensen, S. T.** (2019). Cellular  
640 signalling by primary cilia in development, organ function and disease. *Nat. Rev. Nephrol.* **15**, 199–219.
- 641 **Balderhaar, H. J. kleine and Ungermann, C.** (2013). CORVET and HOPS tethering complexes – coordinators of  
642 endosome and lysosome fusion. *J. Cell Sci.* **126**, 1307–1316.
- 643 **Blacque, O. E., Scheidel, N. and Kuhns, S.** (2018). Rab GTPases in cilium formation and function. *Small*  
644 *GTPases* **9**, 76–94.
- 645 **Breslow, D. K., Hoogendoorn, S., Kopp, A. R., Morgens, D. W., Vu, B. K., Kennedy, M. C., Han, K., Li, A.,**  
646 **Hess, G. T., Bassik, M. C., et al.** (2018). A CRISPR-based screen for Hedgehog signaling provides  
647 insights into ciliary function and ciliopathies. *Nat. Genet.* **50**, 460–471.
- 648 **Brett, C. L., Plemel, R. L., Lobingier, B. T., Vignali, M., Fields, S. and Merz, A. J.** (2008). Efficient termination of  
649 vacuolar Rab GTPase signaling requires coordinated action by a GAP and a protein kinase. *J. Cell Biol.*  
650 **182**, 1141–1151.
- 651 **Bröcker, C., Kuhlee, A., Gatsogiannis, C., kleine Balderhaar, H. J., Hönscher, C., Engelbrecht-Vandré, S.,**  
652 **Ungermann, C. and Raunser, S.** (2012). Molecular architecture of the multisubunit homotypic fusion and  
653 vacuole protein sorting (HOPS) tethering complex. *Proc. Natl. Acad. Sci.* **109**, 1991–1996.
- 654 **Clement, C. A., Ajbro, K. D., Koefoed, K., Vestergaard, M. L., Veland, I. R., Henriques de Jesus, M. P. R.,**  
655 **Pedersen, L. B., Benmerah, A., Andersen, C. Y., Larsen, L. A., et al.** (2013). TGF- $\beta$  signaling is  
656 associated with endocytosis at the pocket region of the primary cilium. *Cell Rep.* **3**, 1806–1814.
- 657 **De Leo, M. G., Staiano, L., Vicinanza, M., Luciani, A., Carissimo, A., Mutarelli, M., Di Campli, A., Polishchuk,**  
658 **E., Di Tullio, G., Morra, V., et al.** (2016). Autophagosome–lysosome fusion triggers a lysosomal response  
659 mediated by TLR9 and controlled by OCRL. *Nat. Cell Biol.* **18**, 839–850.
- 660 **Devlin, L. A. and Sayer, J. A.** (2019). Renal ciliopathies. *Curr. Opin. Genet. Dev.* **56**, 49–60.
- 661 **Doyno, C., Sobieraj, D. M. and Baker, W. L.** (2021). Toxicity of chloroquine and hydroxychloroquine following  
662 therapeutic use or overdose. *Clin. Toxicol.* **59**, 12–23.
- 663 **Francis, S. S., Sfakianos, J., Lo, B. and Mellman, I.** (2011). A hierarchy of signals regulates entry of membrane  
664 proteins into the ciliary membrane domain in epithelial cells. *J. Cell Biol.* **193**, 219–233.
- 665 **Ghossoub, R., Molla-Herman, A., Bastin, P. and Benmerah, A.** (2011). The ciliary pocket: a once-forgotten  
666 membrane domain at the base of cilia. *Biol. Cell* **103**, 131–144.
- 667 **Goetz, S. C. and Anderson, K. V.** (2010). The primary cilium: a signalling centre during vertebrate development.  
668 *Nat. Rev. Genet.* **11**, 331–344.
- 669 **Hasegawa, J., Iwamoto, R., Otomo, T., Nezu, A., Hamasaki, M. and Yoshimori, T.** (2016). Autophagosome-

- 670 lysosome fusion in neurons requires INPP5E, a protein associated with Joubert syndrome. *EMBO J.* **35**,  
671 1853–1867.
- 672 **Hildebrandt, F., Benzing, T. and Katsanis, N.** (2011). Ciliopathies. *N. Engl. J. Med.* **364**, 1533–1543.
- 673 **Hoffman, H. K. and Prekeris, R.** (2022). Roles of the actin cytoskeleton in ciliogenesis. *J. Cell Sci.* **135**,  
674 jcs259030.
- 675 **Homma, Y., Hiragi, S. and Fukuda, M.** (2021). Rab family of small GTPases: an updated view on their regulation  
676 and functions. *FEBS J.* **288**, 36–55.
- 677 **Hu, J., Wittekind, S. G. and Barr, M. M.** (2007). STAM and Hrs down-regulate ciliary TRP receptors. *Mol. Biol.*  
678 *Cell* **18**, 3277–3289.
- 679 **Hurtado-Lorenzo, A., Skinner, M., El Annan, J., Futai, M., Sun-Wada, G.-H., Bourgoïn, S., Casanova, J.,  
680 Wildeman, A., Bechoua, S., Ausiello, D. A., et al.** (2006). V-ATPase interacts with ARNO and Arf6 in  
681 early endosomes and regulates the protein degradative pathway. *Nat. Cell Biol.* **8**, 124–136.
- 682 **Iaconis, D., Crina, C., Brillante, S., Indrieri, A., Morleo, M. and Franco, B.** (2020). The HOPS complex subunit  
683 VPS39 controls ciliogenesis through autophagy. *Hum. Mol. Genet.* **29**, 1018–1029.
- 684 **Jewett, C. E., Soh, A. W. J., Lin, C. H., Lu, Q., Lencer, E., Westlake, C. J., Pearson, C. G. and Prekeris, R.**  
685 (2021). RAB19 Directs Cortical Remodeling and Membrane Growth for Primary Ciliogenesis. *Dev. Cell* **56**,  
686 325-340.e8.
- 687 **Jiang, P., Nishimura, T., Sakamaki, Y., Itakura, E., Hatta, T., Natsume, T. and Mizushima, N.** (2014). The  
688 HOPS complex mediates autophagosome–lysosome fusion through interaction with syntaxin 17. *Mol. Biol.*  
689 *Cell* **25**, 1327–1337.
- 690 **Leitch, C. C., Lodh, S., Prieto-Echagüe, V., Badano, J. L. and Zaghoul, N. A.** (2014). Basal body proteins  
691 regulate Notch signaling through endosomal trafficking. *J. Cell Sci.* **127**, 2407–2419.
- 692 **Liu, M., Zhang, W., Li, M., Feng, J., Kuang, W., Chen, X., Yang, F., Sun, Q., Xu, Z., Hua, J., et al.** (2021).  
693 NudCL2 is an autophagy receptor that mediates selective autophagic degradation of CP110 at mother  
694 centrioles to promote ciliogenesis. *Cell Res.* **31**, 1199–1211.
- 695 **Manders, E. M. M., Verbeek, F. J. and Aten, J. A.** (1993). Measurement of co-localization of objects in dual-colour  
696 confocal images. *J. Microsc.* **169**, 375–382.
- 697 **Marshansky, V., Rubinstein, J. L. and Grüber, G.** (2014). Eukaryotic V-ATPase: Novel structural findings and  
698 functional insights. *Biochim. Biophys. Acta BBA - Bioenerg.* **1837**, 857–879.
- 699 **Masson, J. and El Ghouzzi, V.** (2022). Golgi Dysfunctions in Ciliopathies. *Cells* **11**, 2773.
- 700 **Mauthe, M., Orhon, I., Rocchi, C., Zhou, X., Luhr, M., Hijlkema, K.-J., Coppes, R. P., Engedal, N., Mari, M. and  
701 Reggiori, F.** (2018). Chloroquine inhibits autophagic flux by decreasing autophagosome-lysosome fusion.

- 702 *Autophagy* **14**, 1435–1455.
- 703 **McConnachie, D. J., Stow, J. L. and Mallett, A. J.** (2021). Ciliopathies and the Kidney: A Review. *Am. J. Kidney*  
704 *Dis.* **77**, 410–419.
- 705 **McGuire, C., Stransky, L., Cotter, K. and Forgac, M.** (2017). Regulation of V-ATPase activity. *Front. Biosci.*  
706 *Landmark Ed.* **22**, 609–622.
- 707 **Mitchison, H. M. and Valente, E. M.** (2017). Motile and non-motile cilia in human pathology: from function to  
708 phenotypes. *J. Pathol.* **241**, 294–309.
- 709 **Molla-Herman, A., Ghossoub, R., Blisnick, T., Meunier, A., Serres, C., Silbermann, F., Emmerson, C.,**  
710 **Romeo, K., Bourdoncle, P., Schmitt, A., et al.** (2010). The ciliary pocket: an endocytic membrane domain  
711 at the base of primary and motile cilia. *J. Cell Sci.* **123**, 1785–1795.
- 712 **Mondal, K., Porter, H., Cole, J., Pandya, H. K., Basu, S. K., Khanam, S., Chiu, C.-Y., Shah, V., Stephenson, D.**  
713 **J., Chalfant, C. E., et al.** (2022). Hydroxychloroquine Causes Early Inner Retinal Toxicity and Affects  
714 Autophagosome–Lysosomal Pathway and Sphingolipid Metabolism in the Retina. *Mol. Neurobiol.* **59**,  
715 3873–3887.
- 716 **Monfrini, E., Cogiamanian, F., Salani, S., Straniero, L., Fagiolari, G., Garbellini, M., Carsana, E., Borellini, L.,**  
717 **Biella, F., Moggio, M., et al.** (2021a). A Novel Homozygous VPS11 Variant May Cause Generalized  
718 Dystonia. *Ann. Neurol.* **89**, 834–839.
- 719 **Monfrini, E., Zech, M., Steel, D., Kurian, M. A., Winkelmann, J. and Di Fonzo, A.** (2021b). HOPS-associated  
720 neurological disorders (HOPSANDs): linking endolysosomal dysfunction to the pathogenesis of dystonia.  
721 *Brain* **144**, 2610–2615.
- 722 **Moser, J. J., Fritzler, M. J. and Rattner, J. B.** (2009). Primary ciliogenesis defects are associated with human  
723 astrocytoma/glioblastoma cells. *BMC Cancer* **9**, 448.
- 724 **Mullock, B. M., Bright, N. A., Fearon, C. W., Gray, S. R. and Luzio, J.** (1998). Fusion of Lysosomes with Late  
725 Endosomes Produces a Hybrid Organelle of Intermediate Density and Is NSF Dependent. *J. Cell Biol.* **140**,  
726 591–601.
- 727 **Ostrowicz, C. W., Bröcker, C., Ahnert, F., Nordmann, M., Lachmann, J., Peplowska, K., Perz, A., Auffarth, K.,**  
728 **Engelbrecht-Vandré, S. and Ungermann, C.** (2010). Defined Subunit Arrangement and Rab Interactions  
729 Are Required for Functionality of the HOPS Tethering Complex. *Traffic* **11**, 1334–1346.
- 730 **Pedersen, L. B., Veland, I. R., Schröder, J. M. and Christensen, S. T.** (2008). Assembly of primary cilia. *Dev.*  
731 *Dyn. Off. Publ. Am. Assoc. Anat.* **237**, 1993–2006.
- 732 **Pierce, N. W. and Nachury, M. V.** (2013). Cilia grow by taking a bite out of the cell. *Dev. Cell* **27**, 126–127.
- 733 **Podinovskaia, M. and Spang, A.** (2018). The Endosomal Network: Mediators and Regulators of Endosome

- 734 Maturation. In *Endocytosis and Signaling* (ed. Lamaze, C.) and Prior, I.), pp. 1–38. Cham: Springer  
735 International Publishing.
- 736 **Rao, Y., Hao, R., Wang, B. and Yao, T.-P.** (2014). A Mec17-Myosin II Effector Axis Coordinates Microtubule  
737 Acetylation and Actin Dynamics to Control Primary Cilium Biogenesis. *PLoS ONE* **9**, e114087.
- 738 **Rattner, J. B., Sciore, P., Ou, Y., van der Hoorn, F. A. and Lo, I. K. Y.** (2010). Primary cilia in fibroblast-like type  
739 B synoviocytes lie within a cilium pit: a site of endocytosis. *Histol. Histopathol.* **25**, 865–875.
- 740 **Reiter, J. F. and Leroux, M. R.** (2017). Genes and molecular pathways underpinning ciliopathies. *Nat. Rev. Mol.*  
741 *Cell Biol.* **18**, 533–547.
- 742 **Sanderson, L. E., Lanko, K., Alsagob, M., Almass, R., Al-Ahmadi, N., Najafi, M., Al-Muhaizea, M. A., Alzaidan,**  
743 **H., AIDhalaan, H., Perenthaler, E., et al.** (2021). Bi-allelic variants in HOPS complex subunit VPS41  
744 cause cerebellar ataxia and abnormal membrane trafficking. *Brain* **144**, 769–780.
- 745 **Schindelin, J., Arganda-Carreras, I., Frise, E., Kaynig, V., Longair, M., Pietzsch, T., Preibisch, S., Rueden, C.,**  
746 **Saalfeld, S., Schmid, B., et al.** (2012). Fiji: an open-source platform for biological-image analysis. *Nat.*  
747 *Methods* **9**, 676–682.
- 748 **Schoppe, J., Mari, M., Yavavli, E., Auffarth, K., Cabrera, M., Walter, S., Fröhlich, F. and Ungermann, C.**  
749 (2020). AP $\beta$ 3 vesicle uncoating occurs after HOPS $\beta$  dependent vacuole tethering. *EMBO J.* **39**,
- 750 **Schrezenmeier, E. and Dörner, T.** (2020). Mechanisms of action of hydroxychloroquine and chloroquine:  
751 implications for rheumatology. *Nat. Rev. Rheumatol.* **16**, 155–166.
- 752 **Seals, D. F., Eitzen, G., Margolis, N., Wickner, W. T. and Price, A.** (2000). A Ypt/Rab effector complex  
753 containing the Sec1 homolog Vps33p is required for homotypic vacuole fusion. *Proc. Natl. Acad. Sci.* **97**,  
754 9402–9407.
- 755 **Sinka, R., Gillingham, A. K., Kondylis, V. and Munro, S.** (2008). Golgi coiled-coil proteins contain multiple  
756 binding sites for Rab family G proteins. *J. Cell Biol.* **183**, 607–615.
- 757 **Sorokin, S. P.** (1968). Reconstructions of Centriole Formation and Ciliogenesis in Mammalian Lungs. *J. Cell Sci.* **3**,  
758 207–230.
- 759 **Steel, D., Zech, M., Zhao, C., Barwick, K. E. S., Burke, D., Demailly, D., Kumar, K. R., Zorzi, G., Nardocci, N.,**  
760 **Kaiyrzhanov, R., et al.** (2020). Loss-of-Function Variants in HOPS Complex Genes VPS16 and VPS41  
761 Cause Early Onset Dystonia Associated with Lysosomal Abnormalities. *Ann. Neurol.* **88**, 867–877.
- 762 **Stenmark, H.** (2009). Rab GTPases as coordinators of vesicle traffic. *Nat. Rev. Mol. Cell Biol.* **10**, 513–525.
- 763 **Szalinski, C. M., Labilloy, A., Bruns, J. R. and Weisz, O. A.** (2014). VAMP7 Modulates Ciliary Biogenesis in  
764 Kidney Cells. *PLoS ONE* **9**, e86425.
- 765 **Tang, Z., Lin, M. G., Stowe, T. R., Chen, S., Zhu, M., Stearns, T., Franco, B. and Zhong, Q.** (2013). Autophagy

- 766 promotes primary ciliogenesis by removing OFD1 from centriolar satellites. *Nature* **502**, 254–257.
- 767 **van der Beek, J., Jonker, C., van der Welle, R., Liv, N. and Klumperman, J.** (2019). CORVET, CHEVI and  
768 HOPS – multisubunit tethers of the endo-lysosomal system in health and disease. *J. Cell Sci.* **132**,  
769 jcs189134.
- 770 **van der Welle, R. E. N., Jobling, R., Burns, C., Sanza, P., van der Beek, J. A., Fasano, A., Chen, L.,**  
771 **Zwartkruis, F. J., Zwakenberg, S., Griffin, E. F., et al.** (2021). Neurodegenerative VPS41 variants inhibit  
772 HOPS function and mTORC1-dependent TFEB/TFE3 regulation. *EMBO Mol. Med.* **13**, e13258.
- 773 **Wartosch, L., Günesdogan, U., Graham, S. C. and Luzio, J. P.** (2015). Recruitment of VPS33A to HOPS by  
774 VPS16 Is Required for Lysosome Fusion with Endosomes and Autophagosomes. *Traffic Cph. Den.* **16**,  
775 727–742.
- 776 **Wheway, G., Nazlamova, L. and Hancock, J. T.** (2018). Signaling through the Primary Cilium. *Front. Cell Dev.*  
777 *Biol.* **6**, 8.
- 778 **Willenborg, C., Jing, J., Wu, C., Matern, H., Schaack, J., Burden, J. and Prekeris, R.** (2011). Interaction  
779 between FIP5 and SNX18 regulates epithelial lumen formation. *J. Cell Biol.* **195**, 71–86.
- 780 **Yamamoto, Y. and Mizushima, N.** (2021). Autophagy and Ciliogenesis. *JMA J.* **4**, 207–215.
- 781 **Yamamoto, Y., Chino, H., Tsukamoto, S., Ode, K. L., Ueda, H. R. and Mizushima, N.** (2021). NEK9 regulates  
782 primary cilia formation by acting as a selective autophagy adaptor for MYH9/myosin IIA. *Nat. Commun.* **12**,  
783 3292.

784 **Main Figure Legends**

785

786 **Figure 1: Impaired lysosomal fusion disrupts actin cortical clearing and primary ciliogenesis.**

- 787 A. Parental control wild-type (WT), Vps41 KO, or chloroquine-treated (+CQ) MDCK cells, stained with  
788 LysoTracker to label late endosomes and lysosomes (LE/Ls) and Hoechst to label nuclei. Both Vps41 KO  
789 and CQ-treated cells show enlarged LE/Ls (examples indicated with arrows). Scale bars 10  $\mu\text{m}$ . Blue color  
790 in microscopy images throughout this manuscript shows Hoechst staining of nuclei.
- 791 B. Mean cross-sectional area of LysoTracker-stained LE/Ls, from experiments as in (A). Each point  
792 represents the mean of technical replicates from one biological replicate. Outlier replicates excluded  
793 (ROUT = 2%). Error bars: S.E.M. P-values: Brown-Forsythe and Welch ANOVA and Dunnett's T3 multiple  
794 comparisons test.
- 795 C. WT, Vps41 KO, or CQ-treated MDCK cells, stained with  $\gamma$ -tubulin antibody to label basal bodies, acetylated  
796  $\alpha$ -tubulin antibody to label primary cilia, and Phalloidin to label actin. Scale bars 10  $\mu\text{m}$ . Upper panels:  
797 maximum intensity projection of Phalloidin; yellow arrows and circles indicate examples of actin cortical  
798 clearing. Lower panels: side view slices of merged channels; white arrows indicate basal bodies. Both  
799 Vps41 KO and CQ-treated cells show reduced clearing of the apical actin cortex around the basal body.
- 800 D. Actin intensity profiles, from images as in lower panels of (C). The clearing of the apical actin cortex above  
801 the basal body is defective in Vps41 KO and CQ-treated cells. Error bars: S.D.
- 802 E. Ratio of cortical actin intensity directly above the basal body (within 0.3  $\mu\text{m}$  laterally) to cortical actin  
803 intensity flanking the basal body (2-4  $\mu\text{m}$  laterally), from the intensity profiles in (D). Error bars: S.E.M. P-  
804 values: Brown-Forsythe and Welch ANOVA and Dunnett's T3 multiple comparisons test.
- 805 F. WT, Vps41 KO, or CQ-treated MDCK cells, stained with Arl13b antibody to label primary cilia (arrows  
806 indicate examples of cilia) and Phalloidin. Scale bars 10  $\mu\text{m}$ . Both Vps41 KO and CQ conditions show a  
807 lack of cilia.
- 808 G. Percent of cells exhibiting an Arl13b-labeled primary cilium, from experiments as in (F). Both Vps41 KO  
809 and CQ treatment impair ciliogenesis. Error bars: S.E.M. P-values: mixed-effects analysis with Geisser-  
810 Greenhouse correction and Šidák's multiple comparisons test.

811

812 **Figure 2: Gp135 cortical clearing and primary ciliogenesis are dependent on actin cortical clearing.**

- 813 A. WT, Vps41 KO, or CQ-treated MDCK cells, stained with gp135 antibody and Phalloidin; maximum intensity  
814 projections, scale bars 10  $\mu\text{m}$ . In WT MDCK, the non-ciliary apical membrane protein gp135 is excluded  
815 from the site where the apical actin cortex is cleared (examples indicated with arrows). In both Vps41 KO  
816 and CQ-treated cells, the lack of a clearing in the actin cortex is accompanied by the lack of an exclusion  
817 zone in gp135.
- 818 B. Fraction of cortical actin remaining above the basal body for all individual cells analyzed, of which the  
819 means of each biological replicate are shown in Fig. 1E. Points represent individual cells; bars represent  
820 median and quartiles.
- 821 C. WT, Vps41 KO, or CQ-treated MDCK cells, stained with Arl13b antibody and Phalloidin. Side views,  
822 examples selected to show cilia (arrows) although cilia are infrequent overall in Vps41 KO and CQ-treated  
823 cells. Scale bars 5  $\mu\text{m}$ . In all three conditions, when a cilium is present, it is associated with a clearing in

824 the apical actin cortex.

825 D. WT MDCK cells stained with Arl13b antibody,  $\gamma$ -tubulin antibody, and Phalloidin; maximum intensity  
826 projections, scale bars 10  $\mu\text{m}$ . White arrows indicate examples of cilia in actin clearings, and yellow arrows  
827 indicate examples of actin clearings without cilia.

828

829 **Figure 3: Disruption of lysosomal fusion impairs ciliogenesis by relocalizing Rab19 to enlarged LEs away**  
830 **from the basal body**

831 A. MDCK cells expressing GFP-Rab19 on WT background with or without CQ treatment, or GFP-Rab19 on  
832 Vsp41 KO background, stained with  $\gamma$ -tubulin antibody, Phalloidin, and Hoechst. Side views, scale bars 5  
833  $\mu\text{m}$ . Basal-body localization of Rab19 is decreased in Vps41 KO and CQ-treated cells.

834 B. Fold enrichment of GFP-Rab19 at the basal body, from experiments as shown in (A). Error bars: S.E.M. P-  
835 values: Brown-Forsythe and Welch ANOVA and Dunnett's T3 multiple comparisons test.

836 C. MDCK cells expressing GFP-Rab19 on a Rab19 KO background with or without CQ treatment (upper  
837 panels), or GFP-Rab19 on a WT or Vps41 KO background (lower panels), stained with LysoTracker. Scale  
838 bars 5  $\mu\text{m}$ . Rab19 shows little localization to LE/Ls under basal conditions, but accumulates on membranes  
839 of enlarged LE/Ls in CQ-treated or Vps41 KO cells.

840 D. Fractional overlap between GFP-Rab19 and LysoTracker, from experiments as in (C). Error bars: S.E.M. P-  
841 values: Brown-Forsythe and Welch ANOVA and Dunnett's T3 multiple comparisons test.

842 E. GFP-Rab19 overexpressing WT, Vps41 KO and CQ-treated MDCK cells, stained with Arl13b antibody and  
843 Phalloidin. Maximum intensity projections, scale bars 10  $\mu\text{m}$ . Arrows point to examples of cilia. Compare to  
844 examples of the non-GFP-Rab19-expressing parental cell lines in Fig. 1.

845 F. Percent of cells with an Arl13b-labeled primary cilium, from experiments as in (E). Data for the non-GFP-  
846 Rab19-expressing cell lines is the same as in Fig. 1, repeated here for comparison to the GFP-Rab19-  
847 overexpressing cell lines. Error bars: S.E.M. P-values: mixed-effects analysis with Geisser-Greenhouse  
848 correction and Šidák's multiple comparisons test. GFP-Rab19 overexpression enhanced ciliation in WT  
849 MDCK, partially rescued ciliation in Vps41 KO, and fully rescued ciliation in CQ-treated cells.

850

851 **Figure 4: Rab19 interacts with the HOPS/CORVET core complex**

852 A. Vps protein subunits of the HOPS and CORVET complexes. HOPS-specific subunits shown in purple,  
853 CORVET-specific subunits in green, and shared core subunits in white.

854 B. Anti-Vps11 western blot of GST-Rab19 immunoprecipitation (IP) assay on WT and Vps41 KO MDCK  
855 lysates, showing that Rab19 interacts with Vps11 regardless of presence of Vps41.

856 C. Anti-Vps11 and anti-Vps41 western blots of GST-Rab19 IP assay on WT and Vsp39-, Vps11-, Vps16-,  
857 Vps18-, and Vps33A-siRNA HEK293T lysates. Knockdown of any one of the core subunits severely  
858 disrupted Vps11 and Vps41 expression levels.

859 D. Anti-Vps11 and anti-Vps41 western blots of GST-Rab19 IP assay on WT and Vsp39-, Vps41-, and  
860 Vps39/41-siRNA HEK293T lysates, and on HEK293T lysates with addition of purified recombinant Rab7,  
861 showing that Rab19-Vps11 interaction is not dependent on Vps39 or Vps41 and is not competitive with  
862 Rab7.

863 E. Anti-GFP western blot of GST-Rab19 IP on HEK293T cells transfected either with Vps8-GFP or with GFP  
864 control, showing that Rab19 interacts with CORVET subunit Vps8.

865

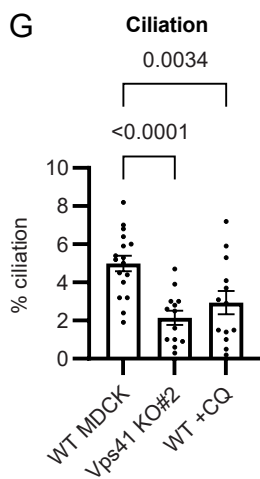
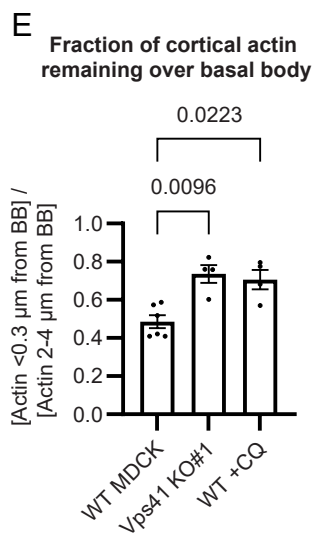
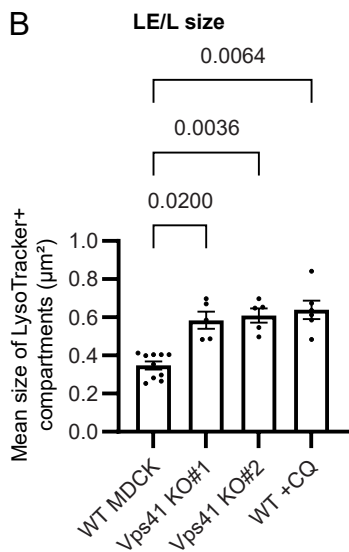
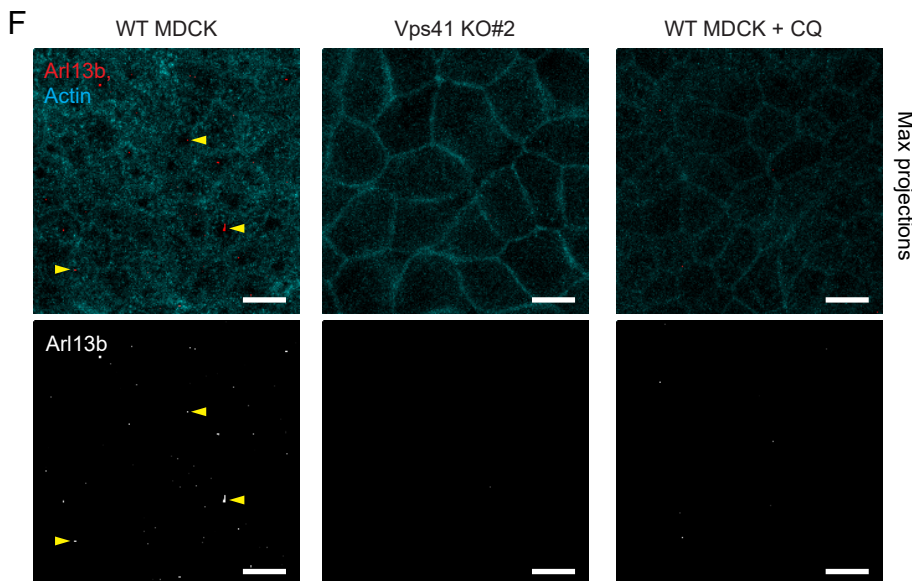
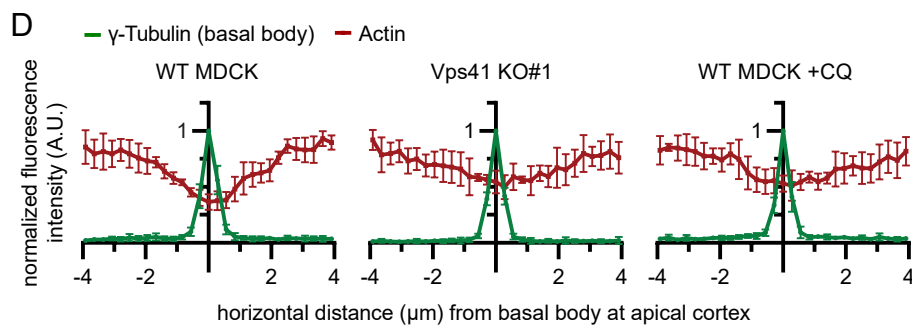
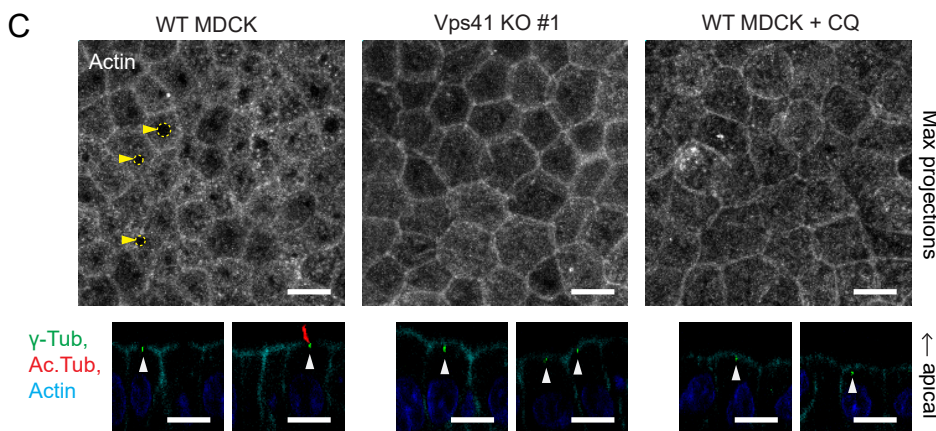
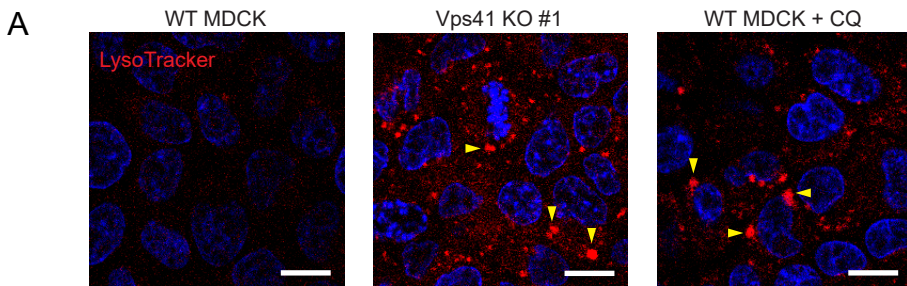
866 **Figure 5: CORVET-containing EEs are found at the site of ciliogenesis.**

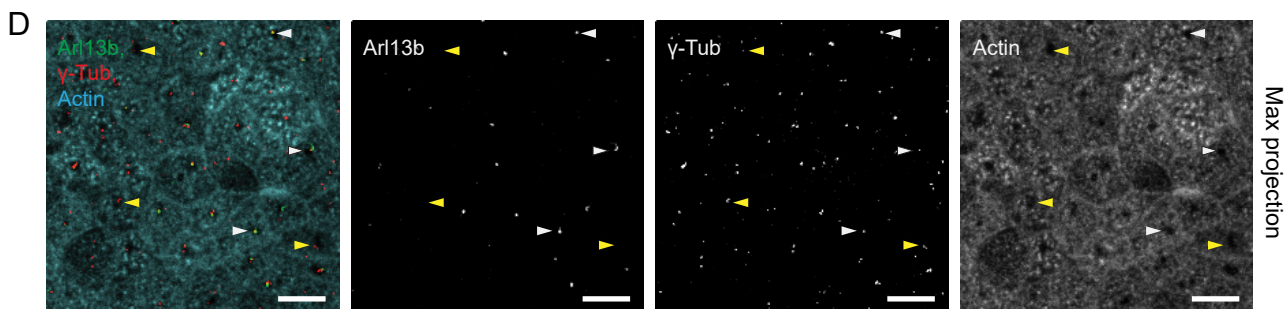
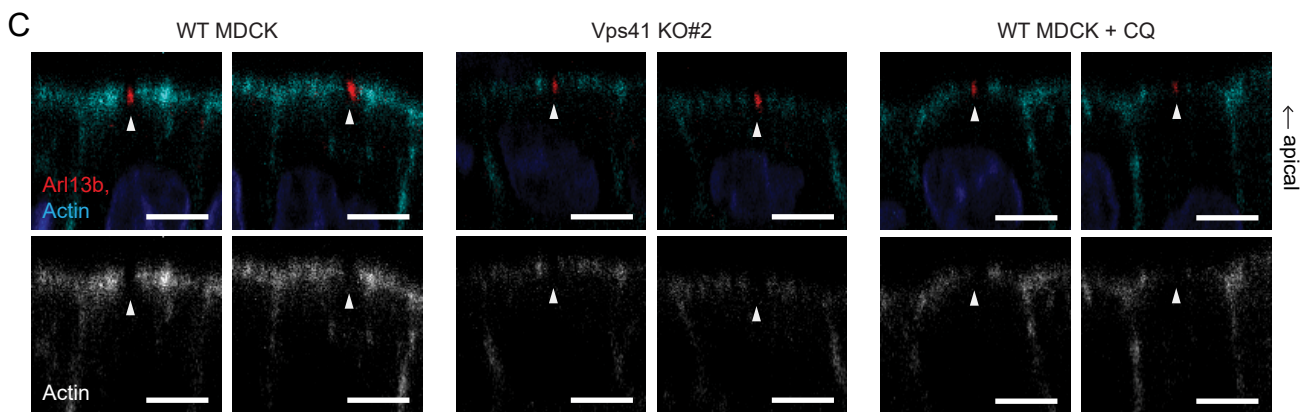
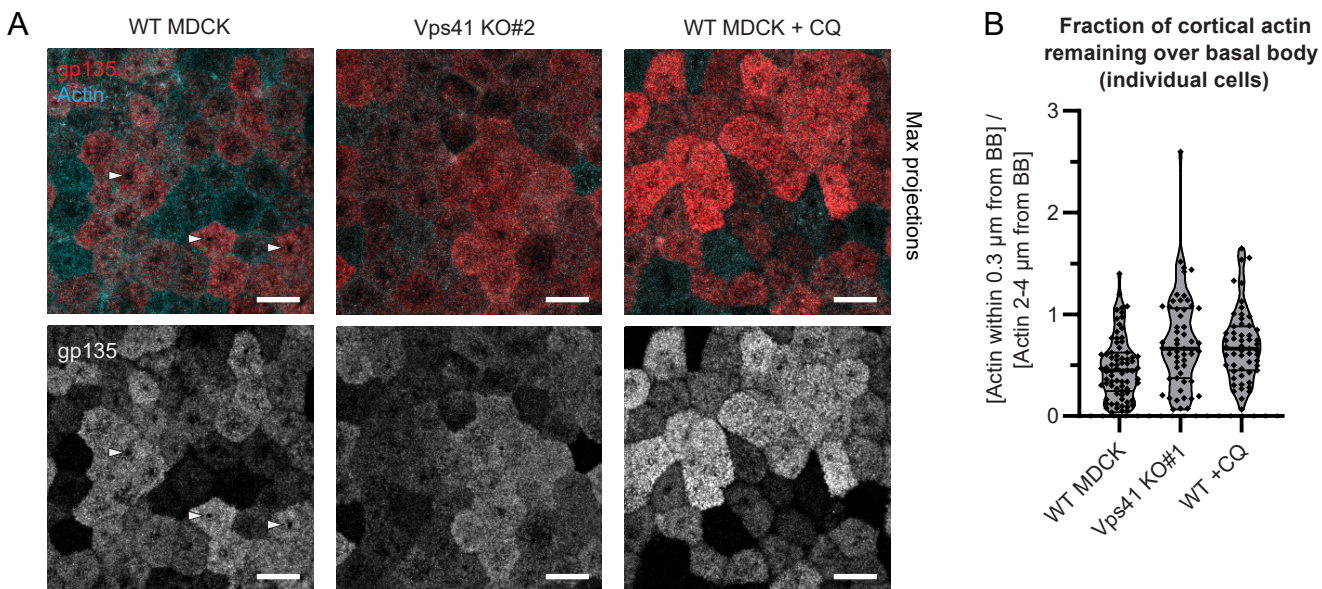
- 867 A. GFP-Rab19 overexpressing WT MDCK cells stained with Vps11 antibody and Phalloidin; side view, scale  
868 bars 5  $\mu$ m. Vps11 overlaps with Rab19 at the periphery of the actin clearing (arrows).
- 869 B. WT MDCK cells stained with Vps11 and EEA1 antibodies and Phalloidin; side view, scale bars 5  $\mu$ m.  
870 Vps11 at the actin clearing is co-labeled with EEA1 (arrows).
- 871 C. WT MDCK cells stained with Vps11 and EEA1 antibodies. Scale bars 5  $\mu$ m. Vps11 colocalizes with EEA1.
- 872 D. WT MDCK cells stained with Vps11 antibody, LysoTracker, and Phalloidin; side view, scale bars 5  $\mu$ m.  
873 Vps11 at the actin clearing (arrow) has little to no co-labeling with LysoTracker.
- 874 E. WT MDCK cells stained with Vps11 antibody and LysoTracker. Scale bars 5  $\mu$ m. Vps11 has little  
875 colocalization with LysoTracker.
- 876 F. WT MDCK cells stained with  $\gamma$ -tubulin and EEA1 antibodies and LysoTracker; side view, scale bars 5  $\mu$ m.  
877 EEA1 but not LysoTracker is observed at the basal body.
- 878 G. Fold enrichment of EEA1 or LysoTracker at the basal body, from experiments as in (F). Error bars: S.E.M.  
879 P-value: Kolmogorov-Smirnov test.
- 880 H. Fractional overlap of Vps11 antibody with EEA1 antibody or with LysoTracker, from images as in (C) and  
881 (E). The majority of Vps11 is colocalized with EEA1 and not with LysoTracker. Error bars: S.E.M. P-values:  
882 Brown-Forsythe and Welch ANOVA and Dunnett's T3 multiple comparisons test.

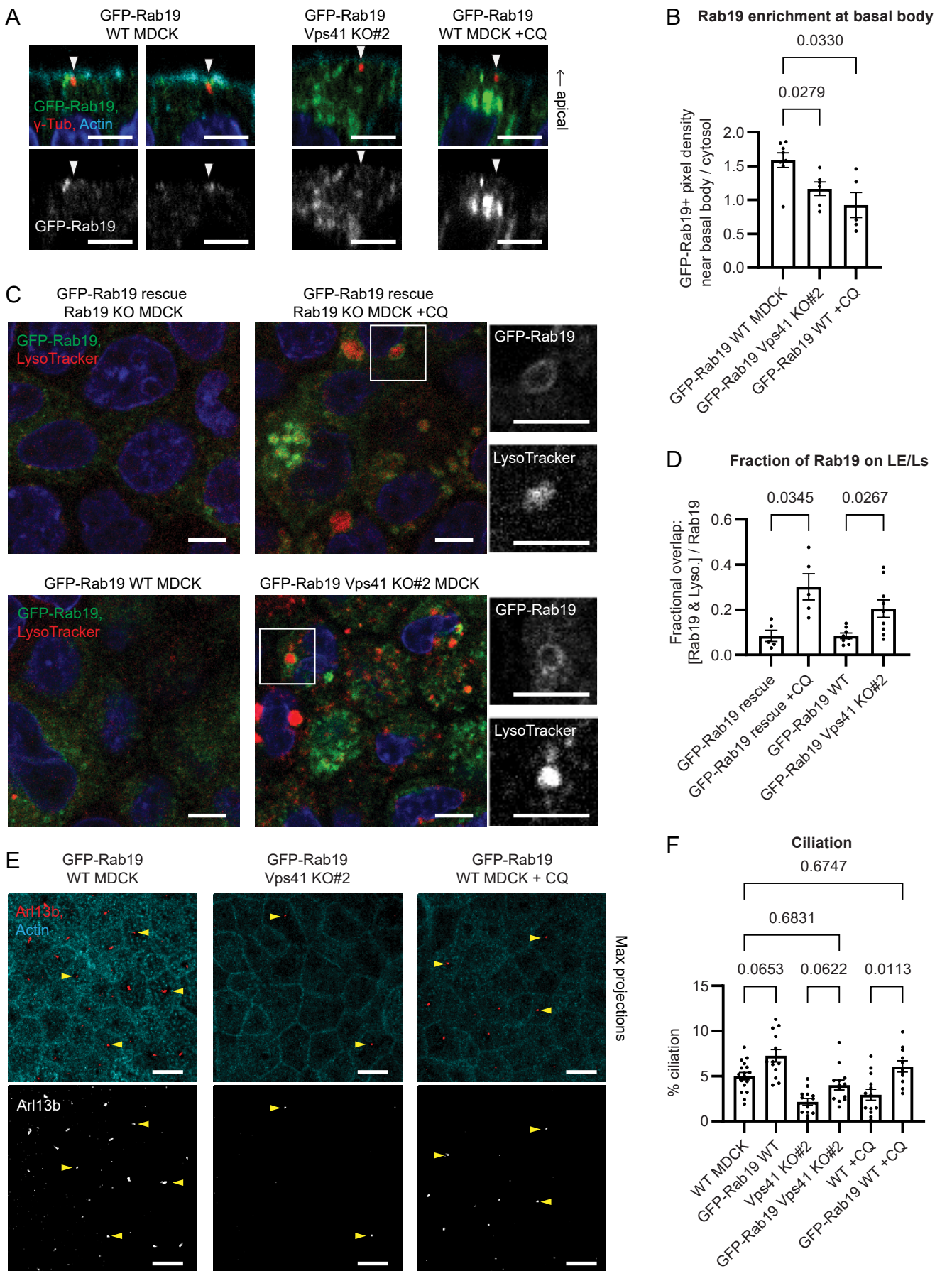
883

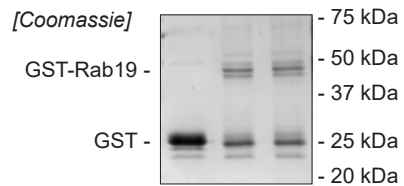
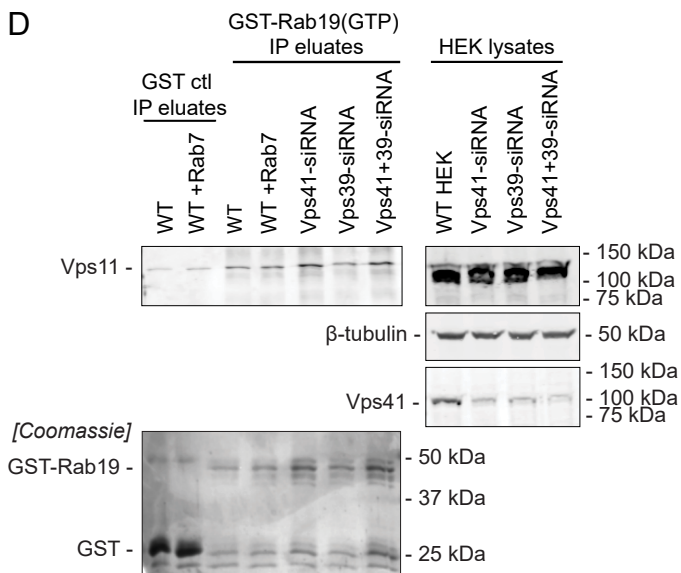
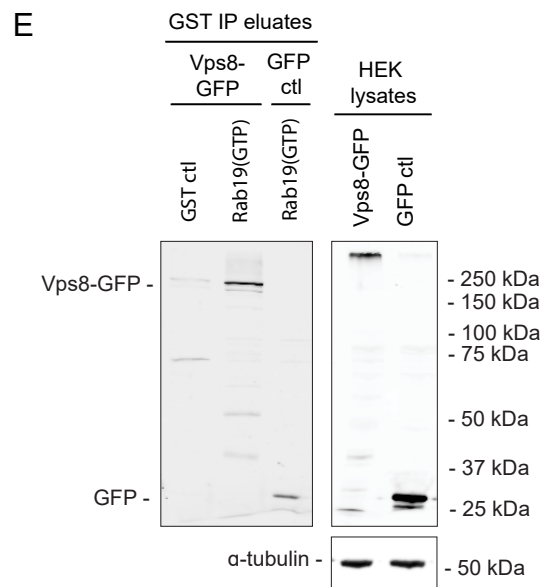
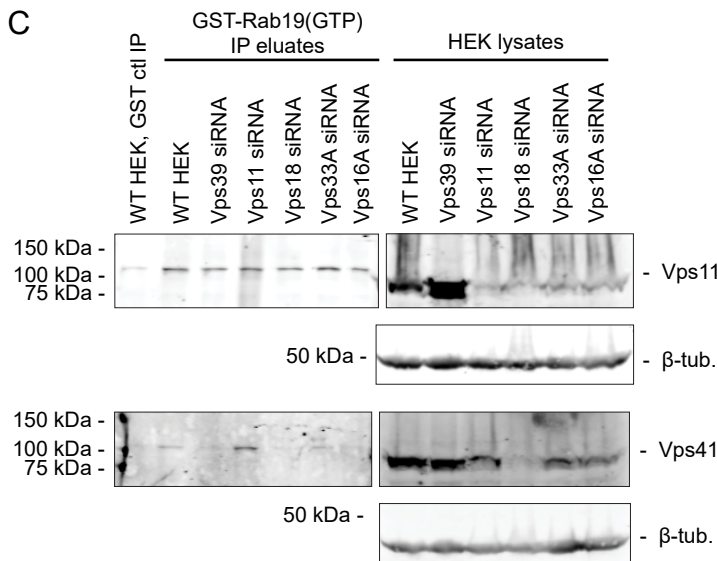
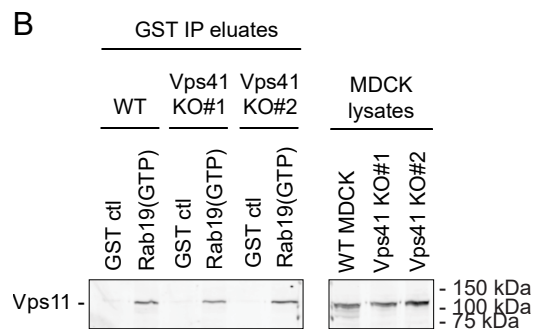
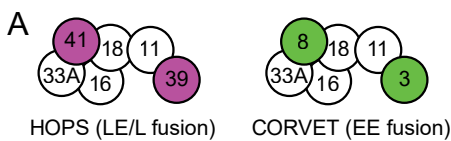
884 **Figure 6: Model: HOPS-dependent lysosomal fusion regulates actin cortical clearing and ciliogenesis by**  
885 **controlling Rab19 availability at the basal body.**

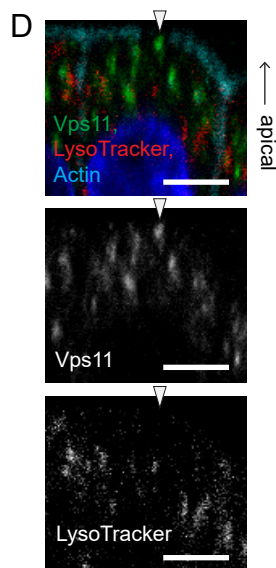
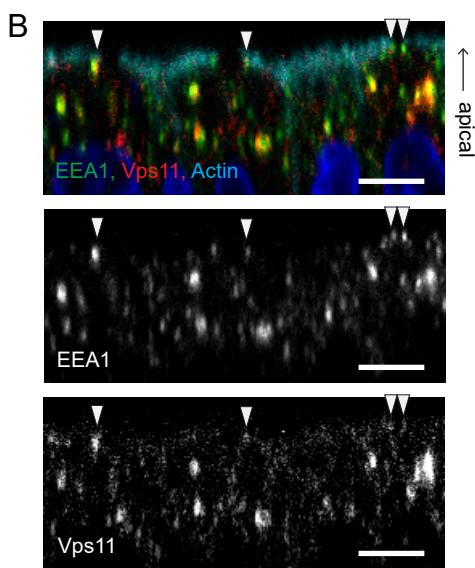
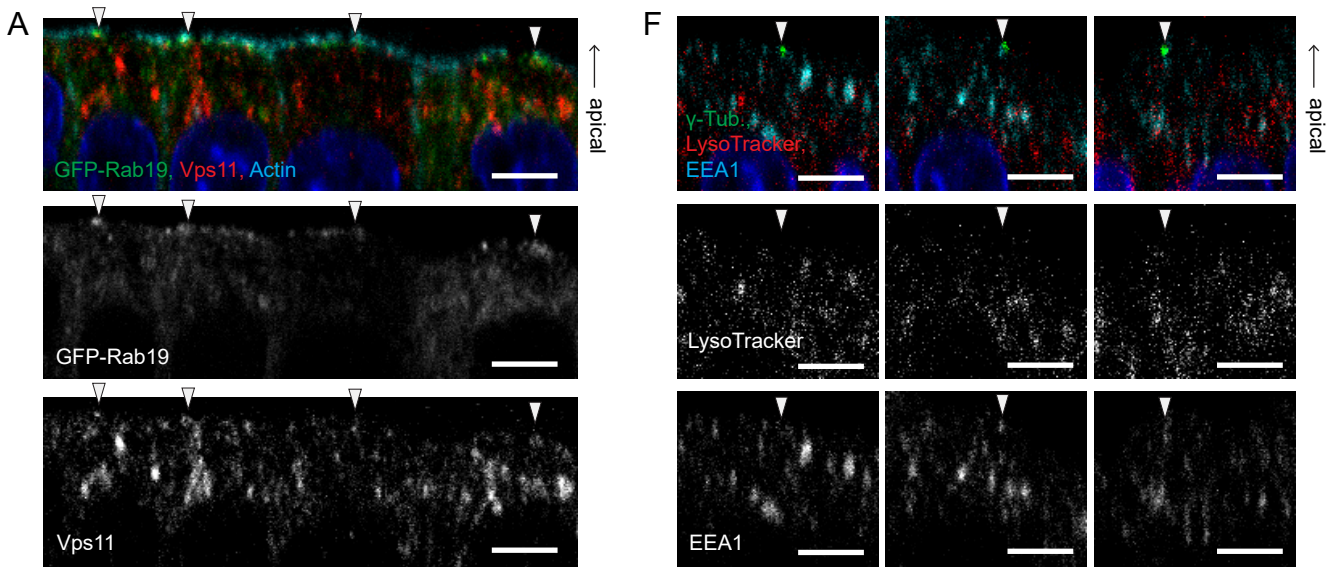
- 886 A. Under normal conditions, a large portion of Rab19 is targeted to the basal body to drive apical actin cortical  
887 clearing and ciliogenesis, while a minor population of Rab19 is transiently recruited to LE membranes and  
888 then cycles off of these membranes following lysosomal fusion. EEs, but not LE/Ls, are enriched at the  
889 basal body.
- 890 B. When lysosomal fusion is impaired by Vps41 KO or CQ treatment, then Rab19 is not released from LEs,  
891 which become enlarged with undegraded cargo. Accumulation of Rab19 on LEs depletes the pool of  
892 Rab19 that can be recruited to the basal body, leading to defects in actin-clearing and ciliogenesis.



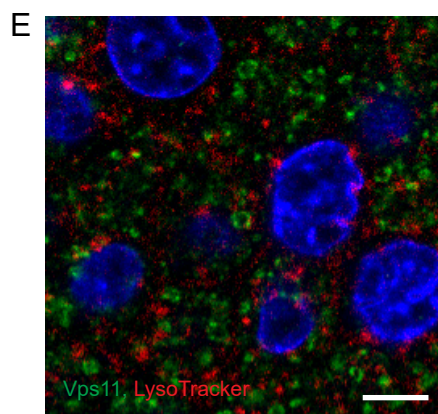
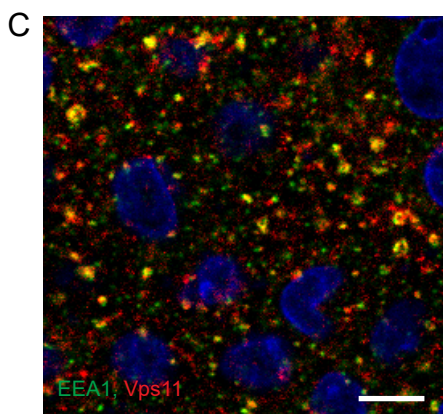
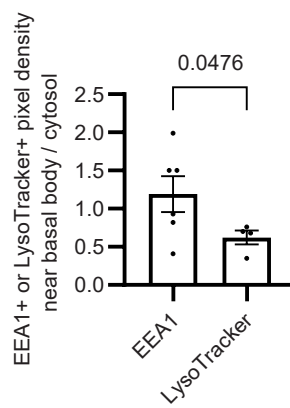




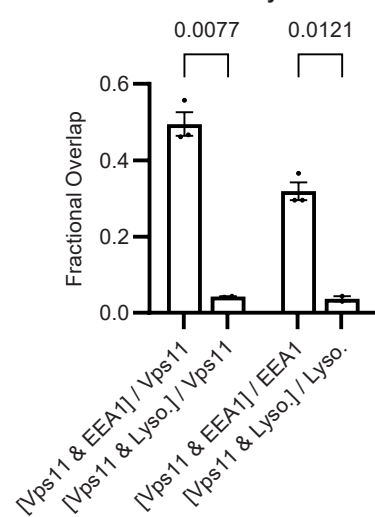




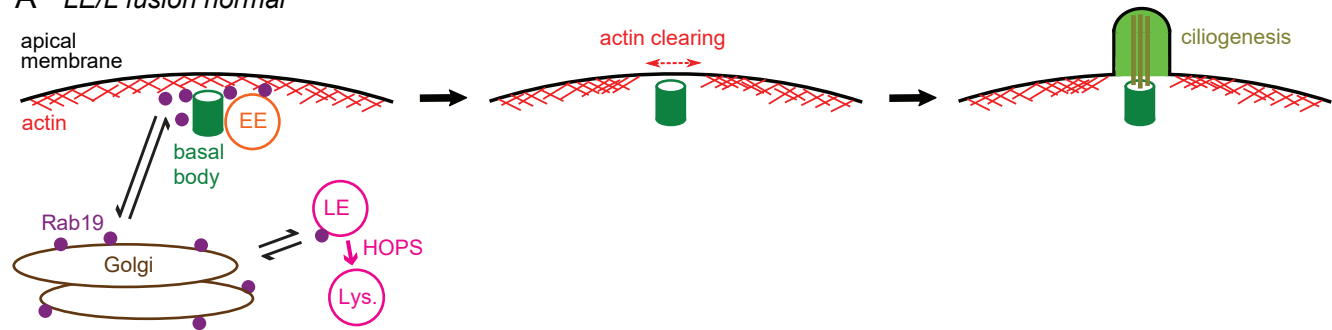
**G** EEA1 vs. LysoTracker enrichment at basal body



**H** Vps11 colocalization with EEA1 vs. LysoTracker



## A *LE/L fusion normal*



## B *LE/L fusion impaired (Vps41 KO or CQ)*

